Practical Considerations in Particle and Object Tracking and Analysis

Jesse Aaron,[1] Eric Wait,[1] Michael DeSantis,[2] and Teng-Leong Chew[1,2,3]

[1]Advanced Imaging Center, Janelia Research Campus, Howard Hughes Medical Institute, Ashburn, Virginia
[2]Light Microscopy Facility, Janelia Research Campus, Howard Hughes Medical Institute, Ashburn, Virginia
[3]Corresponding author: *chewt@janelia.hhmi.org*

The rapid advancement of live-cell imaging technologies has enabled biologists to generate high-dimensional data to follow biological movement at the microscopic level. Yet, the "perceived" ease of use of modern microscopes has led to challenges whereby sub-optimal data are commonly generated that cannot support quantitative tracking and analysis as a result of various ill-advised decisions made during image acquisition. Even optimally acquired images often require further optimization through digital processing before they can be analyzed. In writing this article, we presume our target audience to be biologists with a foundational understanding of digital image acquisition and processing, who are seeking to understand the essential steps for particle/object tracking experiments. It is with this targeted readership in mind that we review the basic principles of image-processing techniques as well as analysis strategies commonly used for tracking experiments. We conclude this technical survey with a discussion of how movement behavior can be mathematically modeled and described. © 2019 by John Wiley & Sons, Inc.

Keywords: cell tracking • diffusion • fluorescence microscopy • image processing • motion analysis • object tracking • single-particle tracking

---

INTRODUCTION

Advances in microscopic imaging technology, fluorescent reporting strategies, and computational capabilities have dramatically expanded biologists' ability to measure dynamic movements within and among living cells, as well as the ability to extract biologically meaningful information from them. However, the complexity of these experiments can prove demanding to many researchers. This unit provides practical guidance that should be considered when attempting to measure and characterize molecular, organelle, and/or cellular dynamic behavior. To date, many approaches for particle and object tracking, with a wide variety of capabilities, have been reported. This unit focuses on the underlying principles, as well as key examples from the literature, and is designed to act as a guide for researchers to formulate an optimal particle- or object-tracking protocol.

The ability to accurately track and characterize cell, organelle, and biomolecule movement is critical across a wide swath of bioscience disciplines, including cell biology, developmental biology, biophysics, and many others (Jin, Heller, Sharma, & Strano, 2009; Keller, Schmidt, Wittbrodt, & Stelzer, 2008; McDole et al., 2018; van der Schaar et al., 2008). The accelerated development of high-speed, automated imaging systems, coupled with the development of genetically encoded fluorescent probes (Dean & Palmer, 2014), have greatly expanded the repertoire and the scope with which biologists are able to perform these important measurements. The
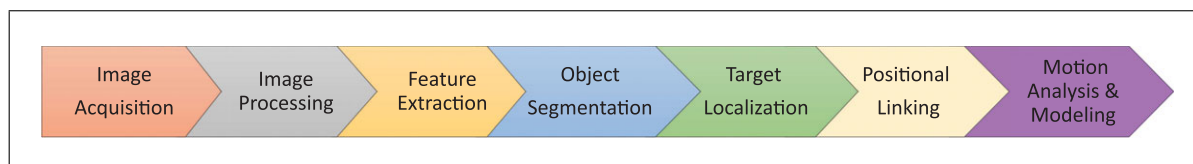
Figure 1 The essential steps involved in target tracking. At each stage, informed decisions and/or assumptions must be implemented to ensure the success of the next analytical step. This overview serves as a practical guide to performing this analysis.

advent of new imaging tools allow biological structures previously beyond the reach of fluorescence microscopy to be tracked — as in the cases of particles that move too fast in three-dimensional (3D) space, low molecular abundance that leads to rapid loss of signal, molecular complexes with multiple components that need to be tracked together, light-sensitive cellular processes that cannot withstand excessive illumination, and even cell lineaging in complex, developing embryos. Likewise, these increasingly complex data sets pose progressively more difficult challenges for accurately tracking the targets of interest and describing the locomotive behavior in mathematical terms.

We use the term "target" here to denote any biological structure to be tracked. Throughout this discussion, "particle" will refer to any target that is smaller than the resolution limit of a microscope. Conversely, "object" will refer to targets that are larger. This distinction is useful, as there are differing strategies for each case. Regardless of the structures being detected, a successful object-tracking analysis involves the following steps, as outlined in Figure 1. Every element in this multistep process is crucial to the subsequent success of target tracking analysis and modeling. Informed decisions and/or wise assumptions must be made at every step to maximize the fidelity and accuracy of the analytical approach. (i) Careful consideration must be given to the selection of fluorophores, image-acquisition parameters, and the appropriate imaging modality. (ii) The acquired images must be appropriately processed to minimize the contribution of noise and improve contrast. This will then facilitate the success of (iii) feature extraction by the software, leading to one of the most important steps of this process: (iv) target recognition, or object segmentation, which categorizes groups of pixels into discrete objects and identifies their relative positions over time. (v) Appropriate target localization step then must be chosen to ensure that the algorithm tracks the biological appropriate reference points in the data set. Only with the suc-

cessful completion of this step can (vi) target tracking begin via positional linking. The approaches involved in the tracking process vary widely, and this is the step that perhaps requires the most informed decisions and assumptions to be made for accurate positional linking of particles. Once the tracking process is completed, (vii) motion analyses can be performed on the numerical data to describe the behavior of the movement through various mathematical models.

A recent effort to evaluate various aspects of target-tracking algorithms was carried out as a competition (Chenouard et al., 2014). In this study, 14 algorithms were submitted to the competition and they were tested against 48 different situations. Chenouard et al. subsequently conclude that no single algorithm is optimal in tackling all the simulated situations. Since the biological microenvironments in which target tracking is performed are even more complicated, it is safe to assume that there is no one method that will fit every experiment. In practice, the various computationally intensive algorithms require some understanding of their fundamental principles before they can be deployed appropriately. It is therefore the goal of this practical guide to explain the underlying concepts of object and particle tracking to provide guidance for a more strategic approach in addressing common biological problems. We will provide an overview of how various factors guide the decision-making process and discuss the best practices at every step. We will conclude by discussing several mathematical models that describe movement behavior. In addition, we have included a list, summarized in Table 1, that defines the commonly used acronyms used in this guide to aid the reader.

STRATEGIES FOR IMAGE ACQUISITION

The first step of the object-tracking process — image acquisition — can ultimately determine the outcome of all the subsequent stages in object tracking. Ironically, it is also the one step that frequently receives insufficient

Table 1 Abbreviations Commonly Used in Particle and Object Tracking and Their Definitions

Terms and phrases	Abbreviation/acronym
Signal-to-noise ratio	SNR
Point-spread function	PSF
Total internal reflection fluorescence	TIRF
Single-particle tracking	SPT
Laplacian of Gaussian	LoG
Difference of Gaussian	DoG
Center of mass	COM
Local nearest neighbor	LNN
Multiple-hypothesis tracking	MHT
Linear assignment problem	LAP
Fluorescence recovery after photobleaching	FRAP
Fluorescence loss in photobleaching	FLIP
Mean squared displacement	MSD
Hidden Markov modeling	HMM

Table 2 Online Resources Listing the Optical Characteristics of Available Fluorescent Proteins and Dyes

URL	Description
https://www.fpbase.org/	Maintained and comprehensive fluorescent protein database, with multiparameter searching and API
https://searchlight.semrock.com/	Spectrum viewer for many fluorescent proteins and dyes, with overlay of filter set spectra, light sources, and detector quantum efficiencies
https://www.thermofisher.com/order/spectra-viewer	Large spectral database of fluorescent dyes, some fluorescent proteins, and overlays of custom excitation and emission filters
https://www.micron.ox.ac.uk/software/spekcheck/	Spectrum viewer with custom loadable fluorophore, light source, filter, and detector profiles. Offers dye optimization routine for a given microscope setup.

consideration during the planning phase (Lambert & Waters, 2017). "Imaging for as long, and as fast, as one could" is not always an advisable strategy.

Selection of Fluorophores

Fluorophore selection is arguably the most important factor that determines image acquisition parameters. Every fluorophore has a *photobleaching rate*, which describes the permanent loss of electrons from the productive cycle of fluorescence emission due to photochemical change (Grimm et al., 2015; Ha & Tinnefeld, 2012; Hoogenboom, van Dijk, Hernando, van Hulst, & Garcia-Parajo, 2005). *Quantum yield* describes the fraction of absorbed photons that a fluorophore re-emits as

fluorescence. Photobleaching rate and quantum yield jointly describe a supremely important factor — *photon budget*. By defining the number of photons that a fluorophore can contribute to the experiment, photon budget determines almost every aspect of image acquisition. It sets the upper limit of the acquisition speed and the imaging duration. By extension, it may also determine whether one can successfully perform imaging in 3D or is limited to the 2D plane. Likewise, it sets the lower limit of molecular abundance one can practically visualize and track on a microscope. A low photon budget can also result in poor signal-to-noise ratio (SNR) and/or exacerbate phototoxicity, as dim fluorophores require higher illumination power and/or exposure time to

reach acceptable SNR. There is decidedly no conceivable reason to choose a fluorophore with poor photon budget, yet it is common to see photon budget being compromised for the convenience of keeping the existing fluorescent labels. Such misguided strategy ultimately levies a huge toll on the success of every subsequent step listed in Figure 1. There are now several powerful online resources that survey the characteristics of available fluorophores and their compatibility with a given microscope setup, as shown in Table 2.

In addition, care should also be taken to assess the degree to which a fluorophore may alter the behavior of a target of interest. For example, the introduction of a genetically encoded fusion tag may perturb the structure of the protein to be imaged, potentially rendering it "nonfunctional" (Snapp, 2005). Even if a target structure is preserved, the addition of a fluorophore may alter the dynamic behavior simply due to the fact that target-fluorophore complex is much larger than the target alone. This may be the case particularly with nanoparticle-based probes such as quantum dots (Kaji, Tokeshi, & Baba, 2007), which can greatly exceed the size/mass of the target to which they are attached.

Setting the Imaging Parameters

Resolution vs. magnification

Contrary to common misconception, it is not always necessary to pursue the highest resolution for object tracking. Resolution is a measurement of the smallest *distance* between two objects that can be separated by the microscope; it is not a measurement of how *small* an object the microscope can detect. If the separation between objects is greater than the diffraction limit, even if the size of the objects is not, no enhanced resolution is necessary. Many object-detection algorithms can achieve higher positional accuracy than what the microscope can resolve. Thus, it is important to make the clear distinction between "accuracy" in object tracking and optical "resolution." In object tracking, accuracy defines the uncertainty of pinpointing the exact position of a target, which is dependent on both the optical resolution of the microscope and the overall brightness of the particle (Thompson, Larson, & Webb, 2002).

Magnification is another parameter to be considered. While increasing magnification does not translate to higher resolution, the effects of magnification play an important role in the accuracy of particle tracking (Carter,

Shubeita, & Gross, 2005). Magnification will ultimately determine the effective pixel size in a digital image. The appropriate distance represented by an image pixel should be sufficiently less than the resolution limit of the microscope to prevent loss of otherwise available image detail. But excessive magnification will create effective pixel sizes that are too small, resulting in fewer photons being collected per pixel. This will severely compromise SNR. The expression below expresses this relationship in terms of image brightness:

$$\text{image brightness} \propto \left(\frac{\text{NA}^4}{\text{magnification}^2} \right)$$

Here, NA refers to the numerical aperture of the imaging system and characterizes the angle range over which an optical system gathers light, and thus also determines the light collection efficiency. As a general guideline, magnification should be chosen such that the point-spread function (PSF) of the microscope will create a 3- to 5-pixel-diameter spot in an image. The PSF is a vital descriptor of any imaging system. It describes how a microscope represents an infinitely small object (at a given wavelength), and thus acts as a measure of the resolving power of the microscope (Hecht, 2002).

Planar vs. volumetric imaging

Not all biological objects move in a 3D space that would require 3D imaging. Volumetric imaging decreases temporal resolution in most microscopes and increases the likelihood of photodamage to the specimen. Objects that are confined to the thin lamella of a well-spread cell, for example, may not require volumetric imaging. Such specimens will benefit more from a simple wide-field or total internal reflection fluorescence (TIRF) microscope. In fact, 3D confocal microscopy would be counterproductive, as precious photons will be unnecessarily rejected by the confocal pinhole. If volumetric imaging is required, then spatial and temporal resolution, as well as the gentleness of illumination of the microscope, will generally have to be adjusted relative to 2D imaging. While confocal microscopes are designed to perform *z* sectioning, it is important to keep in mind that confocal voxels are not isotropic in resolution. The axial resolution can be two to three times larger than the lateral resolution (Schermelleh, Heintzmann, & Leonhardt, 2010). Spinning-disk confocal microscopes can image 3D volumes at higher speed than laser-scanning confocal microscopes, but at

reduced axial resolution often due to pinhole crosstalk (Egner, Andresen, & Hell, 2002).

Recent advances in imaging technologies have provided life scientists with significantly more choices in instrumentation that fit unique experimental needs. In addition to the conventional wide-field and TIRF systems, light-sheet microscopes (Heddleston & Chew, 2016) that employ either Gaussian beams (Huisken & Stainier, 2009; Tomer, Khairy, & Keller, 2011) or Bessel beams (Chen et al., 2014) have greatly improved temporal resolution in volumetric imaging, at a fraction of the photodamage. Volumetric frame rate can be further improved using multifocal microscopes that can capture the entire 3D volume simultaneously with no time lag, a category of microscopes specifically designed for high-speed 3D particle tracking (Abrahamsson et al., 2013). For enhanced spatial resolution, several flavors of structured illumination microscopes (SIMs), such as the instant SIM (iSIM; York et al., 2013) and high-speed SIM driven by a spatial light modulator (Li et al., 2015; Shao, Kner, Rego, & Gustafsson, 2011), have also vastly increased the 3D acquisition speed with enhanced spatial resolution, albeit by compromising the amount of illumination power per time point. And in the case wherein extremely high lateral resolution is required, the recent development of MINFLUX imaging technology can now deliver resolution in the single-digit nanometer range (Balzarotti et al., 2017).

Striking the optimal balance

Tracking accuracy hinges on the precision of target detection and positional linking. These two goals unfortunately do not always work synergistically. Increasing temporal resolution (higher frame rate) will likely translate into poorer SNR, thus jeopardizing the accuracy of object detection and segmentation. On the other hand, increasing acquisition intervals (e.g., to minimize photobleaching) will allot more time for objects to wander away from the position at the previous time point, thus compromising trajectory construction. Since many positional linking approaches are related to the nearest-neighbor algorithm, it is crucial that in single-particle tracking (SPT), the ratio (ρ) between particle displacement and the mean nearest-neighbor distance should be $\rho < 0.5$ (Jaqaman & Danuser, 2009). On the other hand, for larger objects such as individual cells, the frame rate should be set fast enough so that cells migrate less than their average diameter from frame to frame (Zimmer et al., 2006).

IMAGE PROCESSING

Background vs. Noise

Once appropriate images have been acquired, particle or object tracking becomes a computational task. Digital images will always have impurities. These impurities can be attributed to noise, blurring, or any other unwanted signal. Genuine fluorescent signals need to be isolated from the unwanted signal impurities. In this context, "background" (Prewitt & Mendelsohn, 1966) can represent any unwanted signal source, often manifesting as out-of-focus light. "Noise," on the other hand, is a random corruption of any image due to the inherent uncertainty of photon detection (Pawley, 2010; Waters, 2013).

At this stage, it is also important to determine whether the targets of interest can be classified as "particles" or "objects." While many techniques outlined in this section are generally applicable, some are particular to the nature of the target being detected. We can define a particle as a structure that is well represented by a single PSF of the imaging system. In other words, a particle can be treated as a point source of light because its size is less than the resolving power of the imaging system being employed. In most optical setups, this corresponds to targets smaller than half the wavelength of emitted light. An "object," on the other hand, is a target larger than the resolving limit of the microscope being used and can be defined by a connected set of pixels within the image series.

Thresholding

Regardless of the nature of the target being tracked, threshold application is the primary means to separate it from the remainder of the image. In its simplest implementation, a pixel intensity value T is chosen, such that those pixels with an intensity greater than T are considered signals of interest and the rest are ignored. Thresholding can be used to generate binary images, or masks, such that pixel values greater or less than T are assigned a value of 1 or 0, respectively. In this way, thresholding is a way to create infinite contrast between signal and the rest of the image. A key decision should be made either to select a "global" threshold value for all time points in a data set, or to allow different threshold values at each time point. In the absence of significant photobleaching, with targets that display relatively constant intensity, a global threshold may be preferred. Special care should be taken, however, when the targets to be tracked have
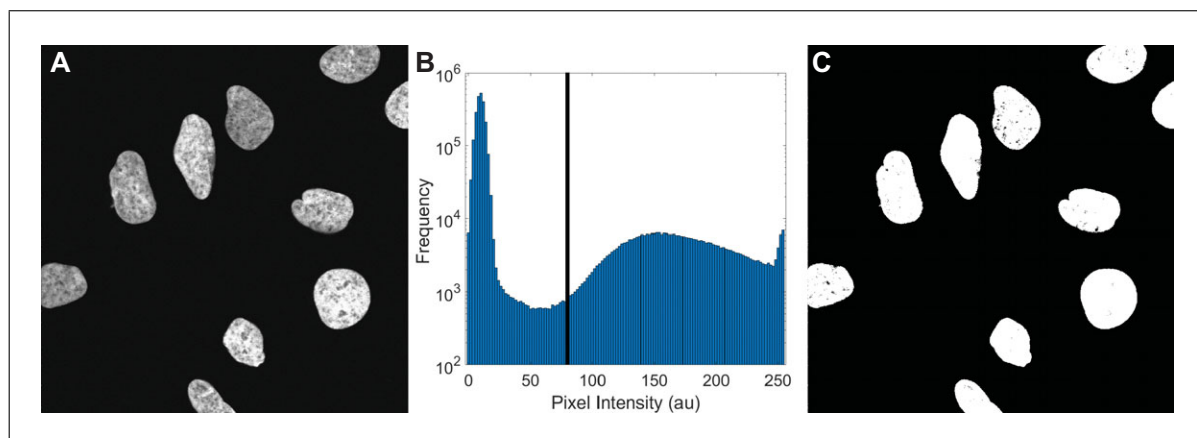
Figure 2 Otsu's thresholding method. (**A**) Fluorescence image of DAPI-stained U2OS cells revealing nuclear morphology, Cell Image Library accession code CIL:40499 (Uhlen et al., 2010). (**B**) The pixel intensity histogram shows the relative distribution of pixel values. Using Otsu's method, an optimal threshold is found that minimizes the variances of both the background and the signals of interest, as denoted by the dashed line. (**C**) Using the Otsu threshold value, a mask can be made such that above-threshold pixels are white, and the rest of the image is black.

widely different intensities across time points. Although the effects of (and possible remedies for) photobleaching have been discussed, targets with widely variable intensity may also occur due to biological reasons that are difficult to control. For example, tracking a dynamically forming multimeric protein complex (Calebiro et al., 2013) or tracking a motile cell expressing calcium sensor (Denninger et al., 2014) may produce such an effect. These complex situations necessitate a varying threshold value over time. In either case, a second key challenge in setting an appropriate threshold level is avoiding user bias. Therefore, automated thresholding is generally the preferred approach.

Automatic thresholding techniques often utilize information from an intensity histogram, which describes the distribution of pixel values in an image. The histogram can be characterized by its peaks, valleys, and curvatures. Typical approaches smooth these features until the histogram resembles a bimodal distribution; consequently, an appropriate threshold level can then be considered the midpoint between these peaks. One widely used algorithm is *Otsu's method* (Otsu, 1979). This technique searches for a threshold level that minimizes the variance (or standard deviation) between above- and below-threshold pixels. As an example, Otsu's method is applied to an image of U2OS cells stained with DAPI in Figure 2A. Figure 2B shows the corresponding pixel intensity histogram with the optimal threshold value indicated by the dashed line. Figure 2C illustrates the results of threshold application with above- and below-threshold pixels shown in white and black, respectively,

revealing a representative mask of cell nuclei. Such image masks at successive time points can then be subjected to further processing, and ultimately tracking analysis, as will be discussed later. However, despite its robustness, Otsu's method can fail when there is a large difference between the number of above- and below-threshold pixels.

Other methods use the concept of image entropy and work by choosing a threshold value that maximizes the entropy difference between signals of interest and the rest of the image (Pun, 1980). These approaches, too, can fail, especially when the sub-threshold signal is nonuniform. As a result, more advanced thresholding methods may be necessary in such cases but are outside the scope of this discussion (Sezgin & Sankur, 2004).

However, even advanced threshold methods may fail in the presence of image impurities, such as noise and background. To combat this, there are image processing techniques that strive to recover the underlying signals of interest. Broadly speaking, these techniques can be classified as denoising methods and background-removal methods. These algorithms can be used individually or in combination. Importantly, however, such processing should not be used in lieu of optimizing the experiment design considerations described earlier.

Image Denoising

As discussed previously, SNR should be maximized in any tracking experiment. However, other considerations may compromise SNR, rendering it low enough to complicate target detection via a simple threshold. It is
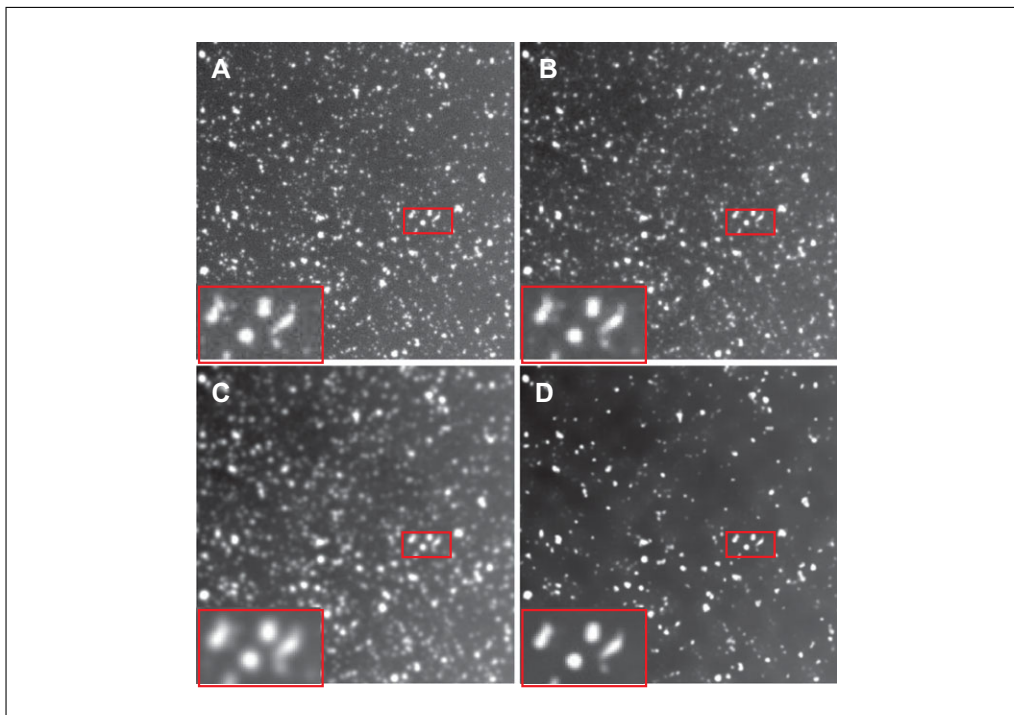
Figure 3 Comparison between denoising techniques. (**A**) An original image containing unwanted noise. (**B**) A median filter is applied to (A), which denoises the image while preserving some edge features. (**C**) A Gaussian filter smooths out noise more than the median filter but at the cost of edge contrast. (**D**) The non-local means filter can smooth out noise while preserving edges.

important to note that no post-acquisition technique will completely negate the effects of poor SNR from image acquisition. Nevertheless, various denoising techniques have been developed to partly ameliorate this common issue.

Denoising methods act to reduce the pixel-to-pixel variability across the image. If the targets to be tracked are large and/or bright, smoothing will make segmentation more effective. However, as targets become smaller and/or dimmer, greater care must be taken to avoid removing them along with the unwanted noise in the image.

Most common denoising strategies survey the surrounding values in the neighborhood of a given pixel. The three most widely used denoising methods are based on *mean*, *median*, and *Gaussian filters*. The neighborhood operations determine the intensity of each pixel in the resulting denoised image. In other words, each pixel value is replaced by one that is more similar to the values around it. For both mean and median filters, the results will be optimal if adjacent pixel values are largely similar in intensity; however, usage of median filters tends to guard better against highly variable local pixel intensities and outperform mean or Gaussian filters at preserving the sharp changes in pixel values that usually denote the boundary

of a particle or object. Gaussian filters assume that bright objects should be brighter in the center with gradual gradients moving outward and thus are ideal for denoising of images containing sub-diffraction sized particles.

Figure 3 illustrates the effects of various denoising algorithms. In Figure 3A, an original simulated image shows variously sized targets with accompanying noise. Figure 3B and C show the results after application of median and Gaussian denoising procedures. Note that while a median filter can better preserve the overall object shape, Gaussian denoising tends to provide smoother images at the expense of edge contrast.

The methods discussed up to this point consider only a localized grouping of pixels. A fourth method, *non-local means*, approaches denoising differently (Buades, Coll, & Morel, 2005). The non-local means strategy considers multiple regions from the image. The method works by first applying a Gaussian filter to the image. Then, regions with similar intensity are grouped together. The center pixel values of these groups are averaged, and the resulting values are used to replace the original pixel intensities. As shown in Figure 3D, non-local means can be a powerful method, as it produces smooth objects while at the same time preserving edge sharpness. However, this
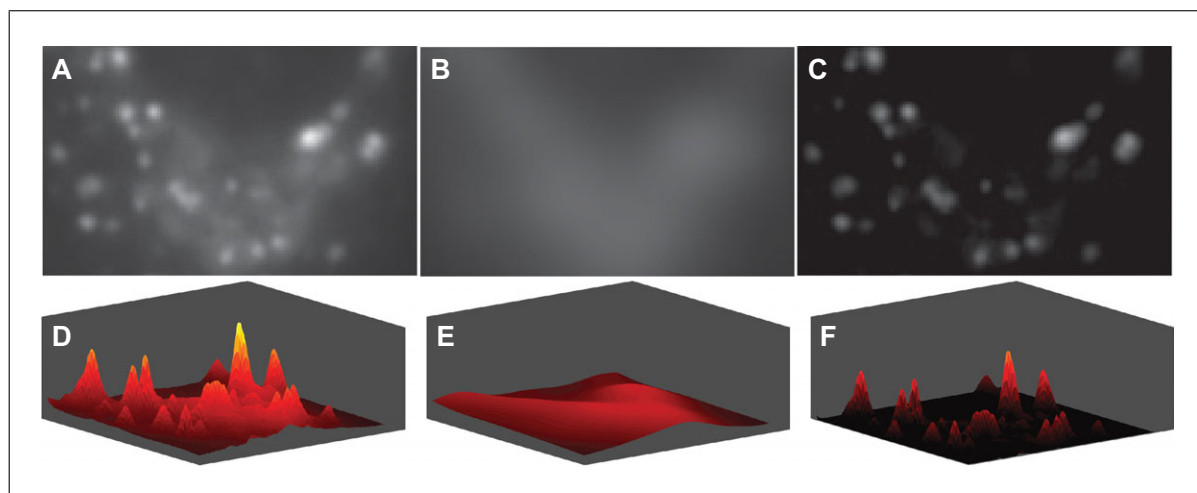
Aaron et al.

Figure 4 Background subtraction. (**A**) An object containing targets of interest with out-of-focus background present; a surface rendering of the same data is shown in (**D**). (**B**) Gaussian blurring of the original image gives an estimate of the background shown; surface rendering is shown in (**E**). Subtracting the background estimate from the original image gives the results shown in (**C**) and (**F**).

method runs the danger of removing small objects. The Gaussian filter size should be set slightly larger than the targets to be detected. However, for SPT, these techniques will tend to remove small targets, which are often the very targets of interest. In conclusion, denoising can aid target detection in poor SNR images. However, any denoising algorithm will come at a cost of poorer spatial and/or temporal resolution.

Removing Out-of-Focus Background

SNR is not the only factor that can complicate target detection. Very often, unwanted signal can originate from out-of-focus light, which it may not be possible to remove at the image acquisition stage. Light from different planes reduces the contrast between the signals of interest and the remaining pixels. While such background signal, in general, will not be constant throughout an image, it is often necessary to assume that background is less structured and/or dimmer than the targets of interest. Many techniques approximate the local background by performing a Gaussian-filter-based blurring of the image, and subtract this estimate from the observed image (Michel, Steinmeyer, Falk, & Harms, 2007). However, care must be taken when selecting the size of the Gaussian filter. Large Gaussian sizes will tend to preserve larger targets of interest at the expense of poorer background removal. In contrast, smaller Gaussian filter sizes will improve background removal at the expense of removing larger targets from the image. In practice, users should optimize background removal with this method by selecting a Gaus-

sian filter size that is slightly larger than the largest target of interest. An analogous method for background subtraction is the *rolling ball* algorithm (Sternberg, 1983). In this implementation, a sliding local minimum filter is used to estimate the background within sub-regions of the image, which is then subtracted. However, the same considerations need to be applied when selecting the appropriate filter size.

Figure 4 illustrates a typical background-subtraction protocol, with the original image displayed in Figure 4A, and a 3D surface rendering of the same image in Figure 4D. An estimated background obtained using Gaussian filter blurring is shown in Figure 4B, with surface representation in Figure 4E. The result of subtracting the estimated background from the original image is shown in Figure 4C and F. Note that background removal substantially increases the contrast between the targets of interest and the remainder of the image.

When considering background, however, it is important to note that unwanted signal may originate not only from out-of-focus planes, but also from the target of interest. As discussed previously, any biological structure will be "convolved" with the PSF of the optical system used to image it. (Hecht, 2002). In practice, therefore, out-of-focus signal could also originate from a target of interest. In this case, the background subtraction methods described above may be ineffective. This problem is especially pronounced in SPT. To effectively remove this unwanted signal, it is necessary to "deconvolve," or decouple, the original image from the underlying PSF.
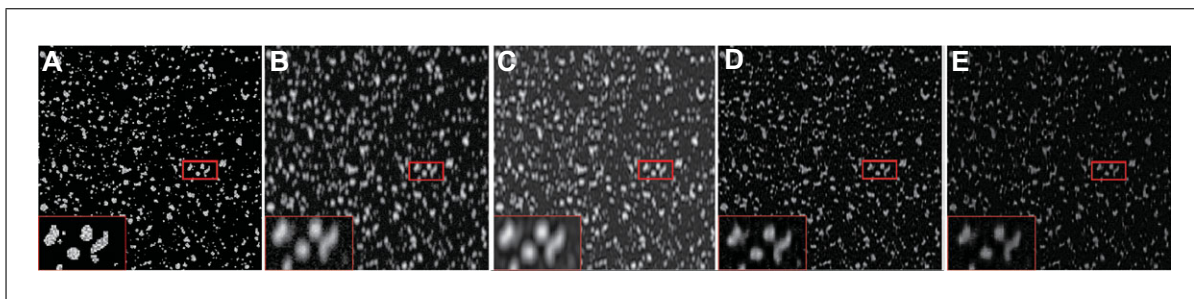
Figure 5 Deconvolution methods. In (**A**), a simulated image is shown that is subjected to blurring and noise corruption in (**B**). (**C**) illustrates the results from Wiener deconvolution, while (**D** and **E**) show the results of deconvolution via the Richardson-Lucy and Blind algorithms, respectively.

Deconvolution

Rather than relying on a user-defined Gaussian filter or rolling ball filter size, deconvolution algorithms estimate the true in-focus fluorophore distribution by attempting to remove the PSF-induced blurring from the acquired image. Broadly speaking, these methods can be divided into "inverse" and "iterative" algorithms.

Inverse algorithms were the first to be introduced and operate via a single calculation step to remove the effect of the underlying PSF on the measured image. A common implementation of this type of technique is called the Wiener filter (Gonzalez & Woods, 2002). However, without suitable modifications, inverse algorithms tend to amplify image noise and create other unwanted artifacts. Thus, many inverse deconvolution algorithms employ the concept of "regularization." This process makes assumptions about the smoothness of the structures in an image that act to constrain the possible pixel values in the final deconvolved image. It also will often assume that pixel values cannot be negative (Takeda, Farsiu, & Milanfar, 2008).

Iterative algorithms were introduced later to improve upon inverse methods such as the Wiener filter. In this case, the deconvolution proceeds through cycles. At each step, the estimated deconvolved image is compared to the previous estimate either until a set number of iterations is completed, or until the current and previous iterations are sufficiently similar. A popular form of this type of deconvolution is the Richardson-Lucy method (Lucy, 1974; Richardson, 1972).

In both Wiener and Richardson-Lucy deconvolution schemes, it is important to obtain an accurate estimate of the PSF of the imaging system being used. Zhang et al. explain how to approximate PSFs for multiple common microscopes (Zhang, Zerubia, & Olivo-Marin, 2007). However, more recently,

"blind" deconvolution algorithms have been introduced that do not have such a requirement. These methods work to estimate both the final deconvolved image and the underlying PSF in tandem to create a suitable image (Ayers & Dainty, 1988; Fish, Brinicombe, Pike, & Walker, 1995).

An example of the results of each of these deconvolution methods are shown in Figure 5. In Figure 5A, a simulated image is shown that is then blurred and subjected to noise corruption such as would be seen with a typical microscope (Fig. 5B). The images in Figure 5C through E reflect the results of Wiener deconvolution, Richardson-Lucy iterative deconvolution, and blind deconvolution, respectively.

As can be seen, iterative algorithms may tend to better recapitulate the original image (Fig. 5A) than the Wiener method. However, key to this result is specifying the correct number of iterations. Specifying too few will insufficiently deblur the image. Specifying too many, however, will tend to amplify noise and ultimately reduce image quality. In addition, Wiener deconvolution retains two important advantages in that it is (i) computationally simpler and (ii) a linear operator. In other words, this method can generate deconvolved images much faster, and more fundamentally, will preserve the relative pixel intensity values from the original image. This linearity may be important when accurate image intensity calculations are necessary. Further, as will be discussed later, preserving intensity linearity may also be important when considering target shape and localization measurements.

Successful background subtraction, denoising, and deconvolution should usually enhance the image quality sufficiently to bring out the real fluorescent signals. Yet, despite the application of these necessary steps, there remain several issues that should be considered before the final target can be appropriately segmented for tracking. In particular, the intensities of the
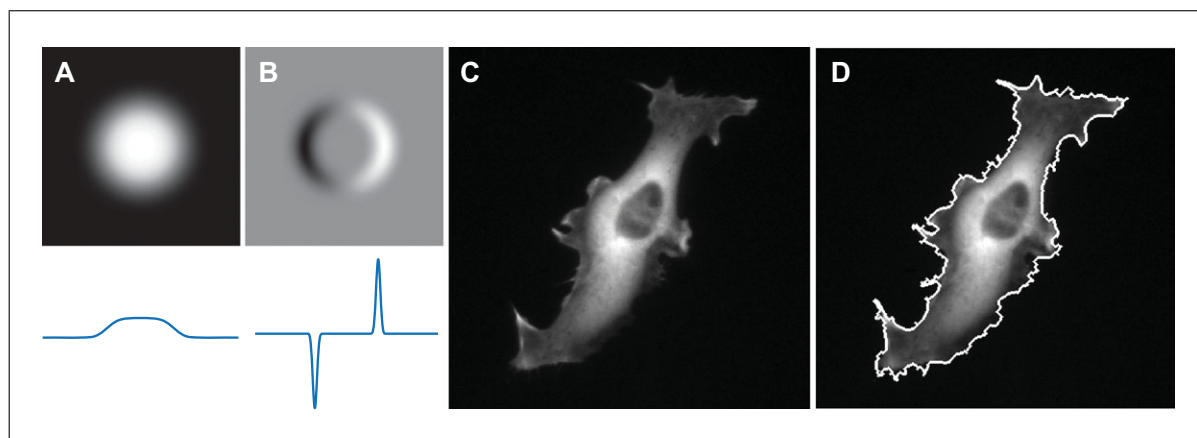
Figure 6 First-order derivative–based edge detection. (**A**) A blurry, circular target with indistinct boundaries. (**B**) Taking the first-order derivative of this image indicates clear maxima and minima that can be used to demarcate the extent of the object. (Intensity profiles for (A) and (B) are shown below in blue.) (**C**) The fluorescence image of a cell can have edges that are difficult to delineate due to other features and fluctuations in intensity across the cell body. (**D**) Application of a Sobel filter (based on a first derivative of the image), in combination with morphometric operations, makes it possible to outline the cell boundary.

biological targets are usually not homogenous. Accordingly, their boundaries may be difficult to define. In these instances, relying on the absolute intensities may not be sufficient to identify the targets. A more effective strategy is to tease out the features of the targets based on local intensity differences.

FEATURE DETECTION

In fluorescent images, structural "features" can be thought of as discontinuities, or sharp gradients of intensity from one pixel region to the next. Therefore, an edge of an object is a powerful feature to leverage for target detection. In contrast to intensity thresholding, edge-detection methods make use of the variation in pixel intensities — not the intensities themselves. This can be useful when the objects of interest lack intensity uniformity or when their edges are difficult to define.

Abrupt changes in intensity can be detected by either first- or second-order derivatives of intensities with respect to position within an image. As illustrated in Figure 6, the power of derivative quantification is that it can reproducibly and mathematically establish the target outline, even for an object with an indistinct boundary. An object with a relatively ill-defined demarcation from the background is shown in Figure 6A, with its intensity profile shown below. Determining the "edge" of this object can prove challenging using an intensity threshold method. However, as shown in Figure 6B, a first-order derivative detects the "upswing" and "downswing" of the intensity gradient of the blurry, circular target, with clear maxima/minima (indicative of inflection

points) that act as an unbiased measure of the extent of the particle. Some edge-detection methods use first-order derivatives that scan an image vertically and horizontally in sequence, then take the positive integer value of the derivatives to establish an outline for the object. Accordingly, when edge-detection methods such as a *Sobel filter* are applied, a threshold is chosen to determine the minimum gradient to keep (Park & Murphey, 2008; Ziou & Tabbone, 1998). First-order derivative–based edge detection using the Sobel filter is further illustrated in Figure 6C and D, with a fluorescence image of a single cell shown in Figure 6C. Note that the "edge" of the cell in this figure is difficult to reproducibly define via simple thresholding, especially if we want to include areas with relatively dim lamella and filopodia. However, the result of a Sobel filter application, in combination with morphometric operators (to be discussed later), is shown in Figure 6D, and indicates the cell boundary that includes these dimmer structures.

Other edge-detection methods can make use of the second spatial derivative of an image, also called the "Laplacian." Figure 7A shows the same object illustrated in Figure 6A and the corresponding second-order derivative in Figure 7B, with intensity profiles below. Plotting the location of the zero-crossing points of the image Laplacian can provide an extremely sensitive measure of the object boundary, shown in Figure 7C.

However, the use of first- and second-order derivatives is also sensitive to pixel intensity fluctuations due to noise. The Laplacian approach, in particular, is generally used only
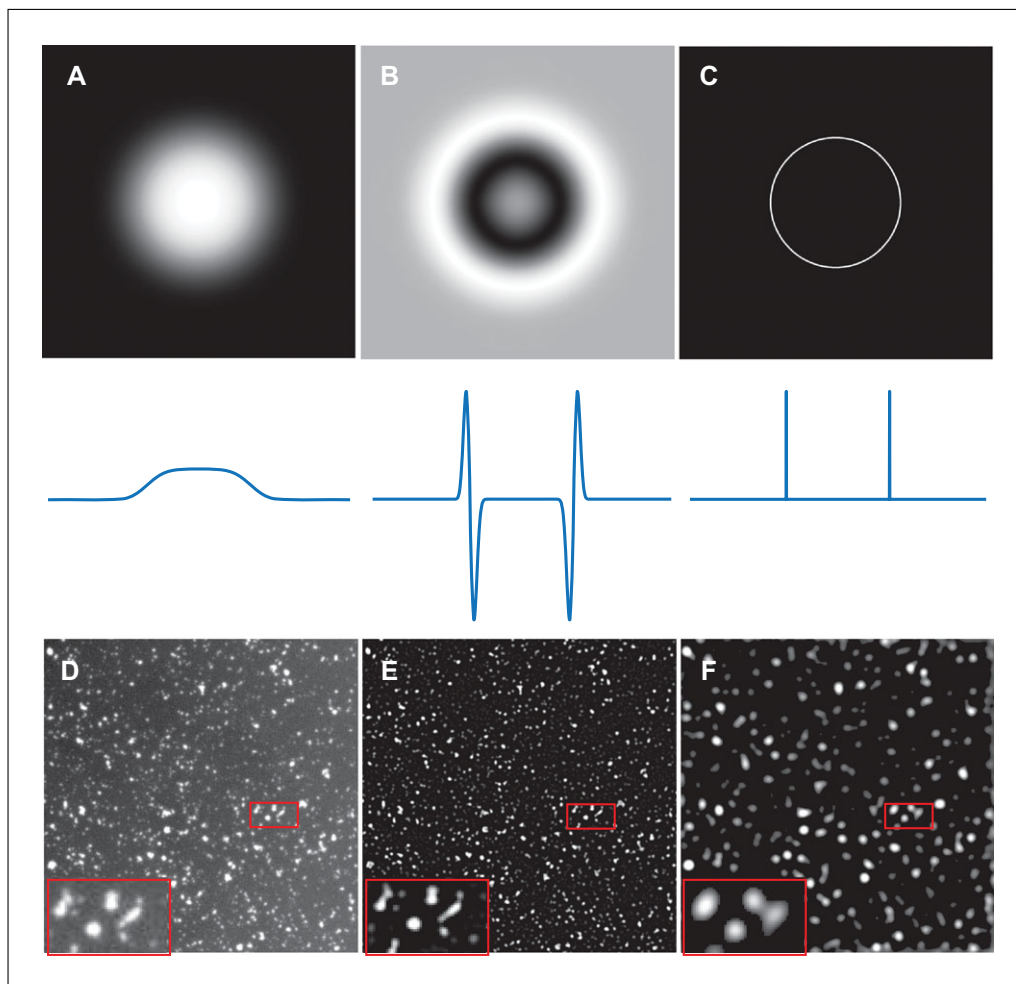
Figure 7 Second-order derivative–based edge detection. (**A**) The same object with relatively indistinct edges shown in Figure 6A. (**B**) The corresponding second-order derivative of (A), also called the Laplacian. (**C**) The zero-crossing points of the second derivative can be used as a particularly sensitive marker of the object boundary. (Intensity profiles for (A), (B), and (C) are shown below in blue.) (**D**) A simulated image showing various targets of interest with relatively low SNR. Application of the LoG detector algorithm with a Gaussian filter size of 1.5 pixels (**E**) and 5 pixels (**F**) indicates that care should be taken when selecting the appropriate filter size to minimize the effects of noise while preserving smaller features.

after application of a denoising filter. In fact, the most common second-order derivative edge detectors are the *Laplacian of Gaussian* (LoG) approach (Marr, Hildreth, & Brenner, 1980; Sotak & Boyer, 1989) and its approximation, the *difference of Gaussian* (DoG) filter (Birch et al., 2010). These algorithms first subject an image to a Gaussian blurring filter as described in the previous section, followed by the Laplacian operator. These methods are especially useful in detecting edges in low-SNR images. Figure 7D shows an image containing targets of interest with relatively low SNR. In Figure 7E, the results from LoG edge detection are shown using a Gaussian filter size of 1.5 pixels. In contrast, the image in Figure 7F shows the same operation but with a 5-pixel Gaussian filter size. As can be

seen, while increasing the Gaussian filter size can better ameliorate the effects of noise in detecting features, it comes at the expense of removing smaller features from the image.

Derivative-based edge detectors can provide a powerful method of feature detection in cases where simple intensity thresholding may fail. By considering relative changes in pixel values, otherwise indistinct or non-uniform objects and particles can be sensitively extracted from even low SNR images. However, it is important to note that not all isolated fluorescent signals are appropriate targets for analysis. It is conceivable, for example, that only objects of a certain size or shape are biologically important targets. To home in on these specific targets while disregarding other above-background fluorescent signals requires

further strategies that would distinguish and detect the unique morphological parameters possessed only by the required targets. In other words, further filtering of the selected targets based on morphology will be required (Meijering, 2012; Ruusuvuori et al., 2010; Smal, Loog, Niessen, & Meijering, 2010; Xing & Yang, 2016).

OBJECT SEGMENTATION

Feature recognition via thresholding or edge detection is often followed by morphometric transforms, even after the processing steps outlined above are performed. Morphometric operations transform binary images so that individual targets are better represented with respect to their overall shapes and boundaries. In other words, they can be used to refine binary masks that exhibit extraneous (and unwanted) features. Morphometric operations, for example, can be used to prune away neurite outgrowth so that the analysis can be focused on the somatic cell bodies. They can also be used to fill cavities in a structure so that imperfections from threshold application do not skew analysis.

Morphometric Operations

Morphometric operations comprise four basic operators: *erosion*, *dilation*, *opening*, and *closing*. As the name implies, erosion removes the outermost pixels at an object boundary, making them shrink in size. In this way, small unwanted objects or small structural features can be removed from the image. Dilation, on the other hand, adds pixels to object boundaries. This can remove erroneous cavities within an object. An opening function consists of erosion followed by dilation and is used to smooth the target contours by eliminating trivial features, small protrusions and breaking narrow connections while preserving relative size. This contrasts with closing (dilation followed by erosion), which is also used to smooth contours but through the converse approach of fusing weakly connected blobs and eliminating holes. These four operations can, in turn, be combined to generate more advanced operations, including *skeletonization*, *thinning*, and *hole filling*, among others (Gonzalez & Woods, 2002).

Depending on target density in the image, the preceding steps may still result in multiple objects that share the same boundary. This can be the case in many biological scenarios, such as tracking individual cells in a migrating epithelial layer or intercalated and overlapping organelles such mitochondria and endo-plasmic reticulum. Separating individual, but not necessarily well-isolated, objects will often demand a *watershed* operation as the last resort for full segmentation.

Watershed

The intensity profile of a fluorescent image can be considered as a landscape, with low-intensity areas represented by valleys and high-intensity areas represented by peaks. Watershed algorithms evaluate the topological structure of an image and subdivide it into multiple regions. As this process was originally described for studying watershed areas, each valley behaves as a water basin, containing pixels surrounding a local minimum or seed point. As the water level rises according to a flooding procedure, the basin grows by adding connected pixels until it reaches the highest peak and interacts with neighboring regions along watershed ridge lines (Beucher & Lantuejoul, 1979).

This description of watersheds works well on grayscale images. However, in the case of object tracking, the targets are already segmented and binary masks created. By definition, a binary masked image has no intensity variations that could create a landscape with peaks and valleys. To facilitate the watershed execution, the flat binary image needs to be transformed into an image with landscape features capable of supporting the "flooding" procedure.

To accomplish this, a distance transformation of the binary masks has to be calculated (Jain, 1989). As shown in Figure 8, the three overlapping objects in Figure 8A can be distance-transformed into a quasi-intensity map as shown in Figure 8B. Distance transformation is accomplished by assigning each pixel a value equivalent to the minimum Euclidean distance to the edge of the mask. The further a given pixel is from the edge, the higher the "intensity" value it will be assigned. Figure 8B is now essentially a landscape with intensity features to be "flooded" by the watershed operation. As a result, the three objects can be segmented (and colored differently) as shown in Figure 8C. Here, a procedure known as connected-component labeling has been performed that assigns a label to each segmented target (i.e., a group of connected pixels). This is useful for identifying all unique targets and for associating various mathematical descriptors (to be discussed in the following section) to each target.

Watershed algorithms perform best with circular objects that have relatively little
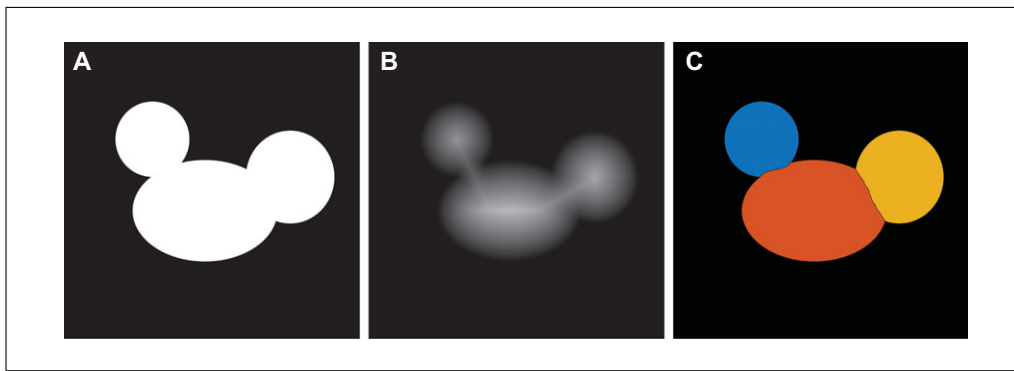
Figure 8 The watershed method can be used to split touching objects. (**A**) A binary mask representing three elliptical objects. The watershed method uses peaks and valleys to identify the boundaries of objects. (**B**) The distance transform of (A), in which each value corresponds to the minimum distance to the edge of the mask. (**C**) The final segmented image.

overlap. These method tends to under-split targets that have large overlaps and over-split irregularly shaped targets, such as multiple cell protrusions or invaginations (Roerdink & Meijster, 2000). Many techniques build upon the original watershed technique to mitigate under- or over-splitting (Lin et al., 2003; Neves, Castro, Tomás, Coimbra, & Proença, 2014; Qi, Xing, Foran, & Yang, 2012; Winter et al., 2018). Ultimately, accurate object segmentation is vital. Errors in the shape or number of targets will ultimately corrupt the results needed in the following stages of tracking (Winter, Mankowski, Wait, Temple, & Cohen, 2016)

TARGET LOCALIZATION

Successful object segmentation brings us to the final step prior to tracking. As we make the critical transition into the actual tracking steps, it is important to explore exactly what a computer algorithm can practically follow. Whether the information one seeks in the tracking experiment is motion directionality and/or velocity, a tracking algorithm requires the true target to be a concise mathematical descriptor — a frame of reference that can be interpreted. Consider a more practical example in which a biologist seeks to track cell movement. In reality, tracking algorithms do not track a "cell" *per se*. Instead, they track a reference point within an object. As a result, the choice of mathematical descriptor will affect how the algorithm localizes the target and thereby the accuracy of the quantitative outcome and data interpretation, as outlined below.

Object Localization

Consider the case of a stationary cell extending large lamella to explore its surround-

ing. Lamellar extension may not necessarily lead to actual cellular locomotion. So, an observer tracking the edge of the lamella as a frame of reference will likely detect movement when another observer tracking the nucleus position will not. The choice of the mathematical descriptor (biological frame of reference) thus matters immensely, and the choice is often hypothesis driven. It is important to understand exactly which part of an object is localized by a chosen mathematical descriptor (Bajcsy et al., 2015; Stegmaier et al., 2016; Winter et al., 2011).

The two most commonly used mathematical descriptors are *centroid* and *center of mass* (COM). As shown in Figure 9, the centroid is the geometric center of the selection — the average of the spatial coordinates of all the pixels in the object. Thus, the centroid of a circle will be its center. The COM, however, is the intensity-weighted average of the coordinates of all the pixels. As shown in Figure 9A and B, if the intensity is not evenly distributed, the COM will gravitate toward the area with higher molecular abundance. More interestingly, the object shape can sometimes shift the COM out of the actual target, as shown in Figure 9C. Therefore, the appropriate mathematical descriptor of target position should be chosen carefully and be kept consistent to prevent erroneous comparisons between data sets.

Particle Localization

While objects can be irregularly shaped when imaged, single particles appear as diffraction-limited spots whose positions should be less ambiguous in comparison (Dimiccoli, Jacob, & Moisan, 2016). Thus, tracking single particles generally only requires determining their positions in 2D or 3D
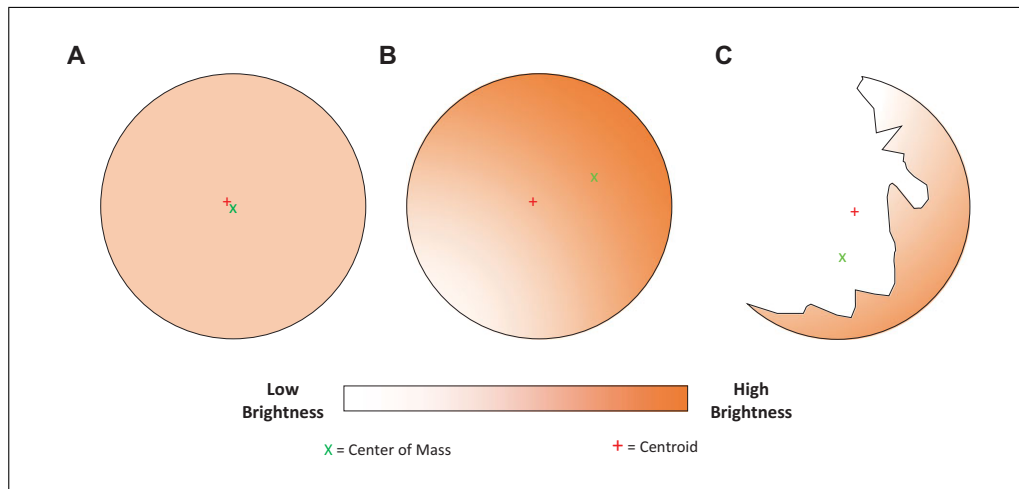
Figure 9 Schematics showing how centroid and center of mass (COM) are affected by the intensity distribution and shape of the target. (**A**) In a target with homogenous intensity, the centroid and COM will coincide. (**B**) In targets with inhomogeneous intensities, however, the centroid and COM will not always overlap, with the COM gravitating towards brighter regions. (**C**) Concave targets can have centroid or COM positions that are outside the boundaries of the target itself.

to reconstruct trajectories. Morphological parameters are ill defined in the case of single particles, as the feature of interest is taken to be the PSF of the imaging system and is considered invariant.

The precision of a particle localization measurement will be one of the most important factors that determine the success of further analysis, as discussed later. The localization of a single particle can, in theory, be determined with an arbitrary precision that depends on the SNR (Bobroff, 1998; Deschout et al., 2014; Kubitscheck, Kückmann, Kues, & Peters, 2000; Thompson et al., 2002). In practice, however, the localization precision of single particles is generally limited to >10 nm in the x and y directions, with z-localization precision typically two- to fourfold worse (Huang, Wang, Bates, & Zhuang, 2008; Juette et al., 2008; Pavani et al., 2009), although there are notable exceptions that display nearly equal localization precision in all three dimensions (Shtengel et al., 2009).

Multiple algorithms exist, with increasing complexity and precision, for localizing single particles. (i) *Manual tracking*: whereby the user simply infers the position of the particle without any further criteria, as in plugins for ImageJ (Rueden et al., 2017) that can record movements between frames. (ii) *Local maximum selection*: pixel intensities are evaluated following grayscale dilation, and the brightest is selected as the location of the particle to the nearest pixel (Jain, 1989; Sbalzarini & Koumoutsakos, 2005). (iii) *COM* (as discussed above): particle position can be inferred to

within sub-pixel precision, but with high sensitivity to noise.

While the methods above can provide good approximate particle positions, in practice more precise calculations are usually employed. (iv) Using *radial-based approaches*, the lateral position of a particle is geometrically calculated from the convergence of multiple lines drawn along the intensity gradient of a single PSF. The intersecting point of all such lines will indicate the location of a single particle with high precision (Parthasarathy, 2012). (vi) *Least-squares Gaussian fitting* is the most common approach. In this method, the intensity distribution of the spot is fit to a 2D Gaussian function:

$$I_{ij} = I_0 \exp\left[-\frac{(i - x_0)^2}{2\sigma_i^2} - \frac{(j - y_0)^2}{2\sigma_j^2}\right] + \langle b \rangle,$$

where I_0 is the peak intensity, σ_i and σ_j are the standard deviations or widths of the PSF in the x- and y- directions, respectively, $<b>$ is the mean background offset, and x_0 and y_0 represents the particle position in space.

Given an image of immobile enhanced green fluorescent protein (EGFP) molecules as shown in Figure 10A, the intensity profile of a single particle (Fig. 10B) can be well described by a 2D Gaussian function (Fig. 10C). It is important to note that particle movement will naturally introduce blurring that can distort and widen the PSF. Nevertheless, the particle localization can still be calculated with sub-pixel accuracy.
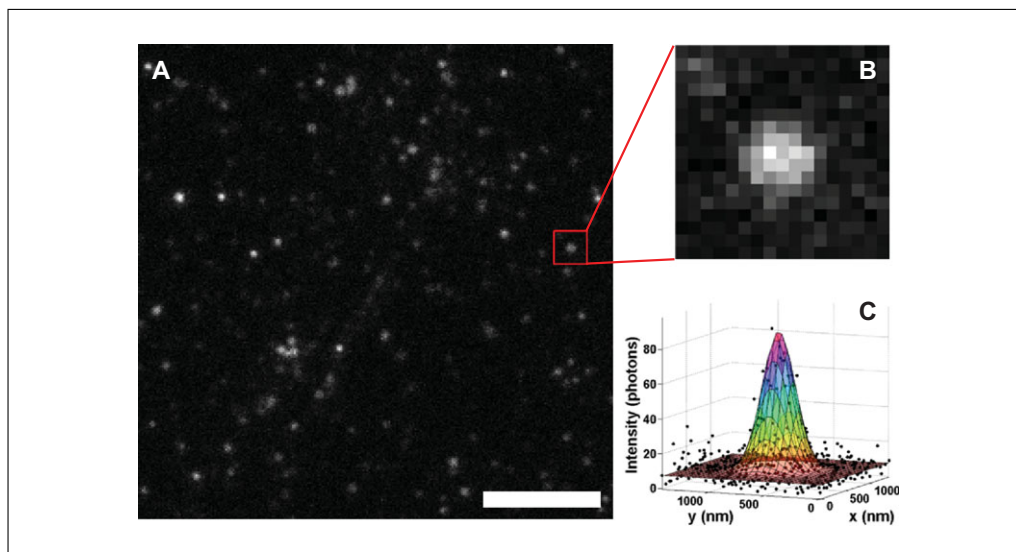
Figure 10 2D Gaussian fitting for particle localization. (**A**) EGFP molecules, appearing as diffraction-limited spots, immobilized on a glass coverslip and imaged using TIRF microscopy. Scale bar is 5 μm. (**B**) A single image (17×17 pixels^2) depicting the PSF for one of the molecules in (A) was selected based on automatic thresholding. (**C**) Corresponding 2D Gaussian fit from which the probable location of the particle along the *x* and *y* dimensions and associated localization precisions are determined.

The precisions associated with these various fitting approaches have been analytically calculated by accounting for various sources of noise (DeSantis, Zareh, Li, Blankenship, & Wang, 2012; Thompson et al., 2002); experiments employing "super-localization" analysis can attain reported accuracies of several nanometers (Manzo & Garcia-Parajo, 2015; Yildiz et al., 2003). (vii) Finally, in *maximum-likelihood estimation* approaches, the intensity distribution of a single particle is fit to a "true," or measured, PSF instead of to a Gaussian approximation. As expected, this procedure can result in higher precision, but it is much more computationally intensive (Mortensen, Churchman, Spudich, & Flyvbjerg, 2010).

POSITIONAL LINKING STRATEGIES

Positional linking relies on all the previously discussed processing techniques and is the first step in connecting targets of interest from sequential moments in time. In this step, the temporal aspect of the analysis is introduced into the process, and trajectories that link target positions between frames are constructed. There are several hurdles that complicate the successful establishment of tracks. In principle, even with successful object segmentation, the accuracy of creating tracks deteriorates when (i) target density increases, (ii) instantaneous (frame-to-frame) displacement distance increases, (iii) time interval be-

tween frames increases, (iv) shape of the object changes, (v) SNR decreases, (vi) intensity of the object changes, (vii) number of potential path-crossings increases, and (viii) motion heterogeneity increases — such as from random movement to one facilitated by molecular motors (Meijering, Smal, & Danuser, 2006). In order to address various combinations of the challenges listed here, a wealth of positional linking algorithms have been developed. It is beyond the scope of this paper to include a comprehensive survey of every algorithm available. However, we will categorize the various methods into groups based on how they perform positional linking to create tracks. It is important to note that no one single algorithm is superior. Thus, some prior understanding of how each type of algorithm functions should greatly help readers in making the best-educated choice.

Overall, tracking algorithms can be roughly classified into the following categories: (i) those employing a local-nearest-neighbor approach; (ii) those using a cost matrix and the linear assignment problem (LAP); and (iii) those making track predictions, for example using Kalman filters.

Local-Nearest-Neighbor Tracking Algorithm

As shown in Figure 11, the local-nearest-neighbor (LNN) method looks for the nearest neighbor of a particle in each successive frame
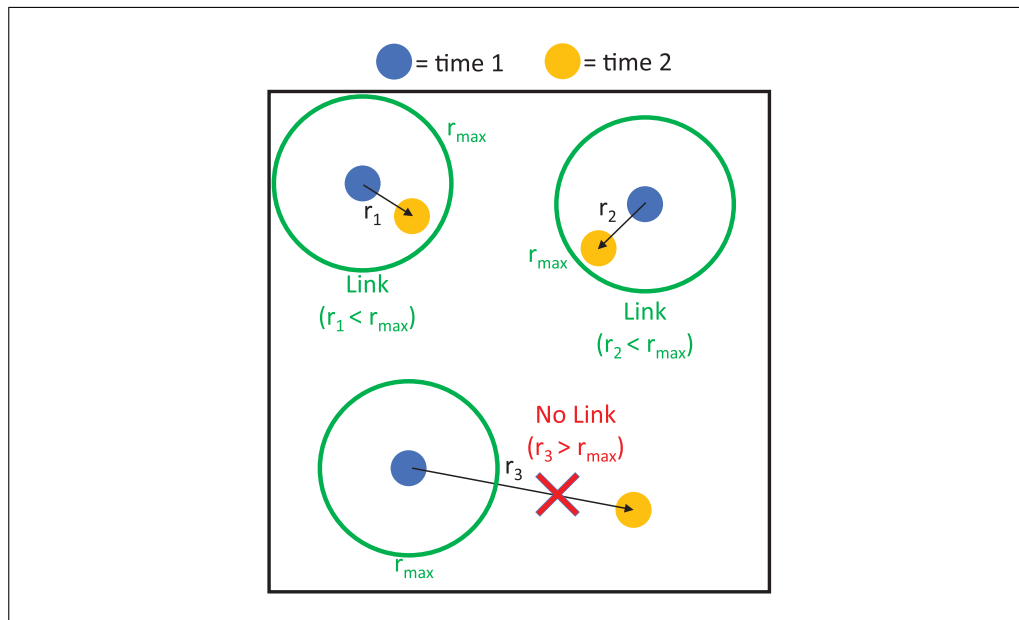
Figure 11 Local nearest neighborhood. The user-defined maximum radius (r_{max}) sets the search radius for the LNN algorithm. The shortest frame-to-frame displacement (hence the term "nearest neighbor") will be linked by the algorithm with a track. This method works well under conditions in which particle density is low.

within the search radius set by the user. The size of the search radius is thus a critical part of the experimental assumptions that need to be made. If an object is detected outside the radius, no link will be made, and the track will be terminated. The unlinked object in this new frame will then be considered a new object (and a new track will begin). As is clear from Figure 11, LNN will fail when (i) the temporal resolution is set too low or the radius is set too short (not adhering to the condition that $\rho < 0.5$, as discussed earlier in the image acquisition section) relative to target speed (Jaqaman & Danuser, 2009), or (ii) the density of targets is too high, such that there are too many candidate targets for the algorithm to make the connection (Crocker & Grier, 1996).

Multiple-Hypothesis Tracking Algorithms: General Overview

Even with images properly processed for subsequent tracking, the problem of following biological movement is complex. Particles or objects can move in and out of the focal plane, merge or divide, engage in near-Brownian movement, move along the same track (as in microtubule-based movement or within a narrow axon), move as a cohort (as in epithelial cell sheet migration), change shape during locomotion, or even change their state of existence by being degraded or synthesized.

The problems commonly encountered in biology call for an algorithm that can con-sider the cumulative scenarios holistically in the system rather than exploring a confined neighborhood limited by a user-defined radius. To overcome this problem, a multiple-hypothesis tracking (MHT) algorithm was first developed as early as 1979 (Reid, 1979). The MHT approach considers all possible target trajectories within the confines of user-defined motion for the entire time-lapse sequence. In doing so, MHT tests all possible "hypotheses" or hypothetical models that can possibly con-struct the trajectory of the targets. Once that computing-intensive, hypotheses-testing task is done, the algorithm chooses as its final solu-tion the scenario with the largest "nonconflict-ing" collection of trajectories. The algorithm will classify a scenario as conflicting if two paths share, in any given frame, the position of the same target. Theoretically, MHT may be the most ideal algorithm; however, it requires computational power that is not practically feasible.

To improve the computational efficiency while harnessing the globally optimal solution offered by the MHT algorithm, several heuris-tic approaches (Chenouard, Bloch, & Olivo-Marin, 2013) have been developed that attempt to divide the computation into two stages by (i) performing many local solutions first in frame-to-frame positional linking, and then (ii) solv-ing the frame-to-frame connection problem in a spatially global manner. We will survey a few that are commonly used and widely available

Cost Matrix and Assignment Problem

		Jobs					
		1	**2**	**3**	**4**	**5**	**6**
Machines	**A**	2.5	5.5	1.0	4.0	3.0	2.0
	B	3.0	6.5	2.0	9.0	3.5	4.0
	C	6.0	9.0	5.0	9.5	6.0	7.5
	D	3.0	7	1.5	5.0	2.0	4.5
	E	1.0	6.0	2.5	6.5	9.5	3.0
	F	6.5	8.5	5.5	8.5	4.5	6.0

Figure 12 Example of a cost matrix, commonly encountered in industrial task assignment. Each different machine may perform the same task but with a different cost. The goal of an assignment problem is to find a way to solve all the problems for the minimal cost.

in shareware such as FIJI (Schindelin et al., 2012) or ImageJ (Rueden et al., 2017).

Cost Matrix and Assignment Problem in Tracking

While there is no one superior approach that can handle all of these challenges, most methods are various permutations of *cost matrix* and *assignment problem*. The concept of the assignment problem was originally devised to deal with the industrial challenge of assigning *n* number of "jobs" to *n* number of "machines" in the most efficient manner (Mulmuley, Vazirani, & Vazirani, 1987). A common problem encountered in industry is how to get the most tasks accomplished for the lowest cost. Imagine a factory with six different machines that can perform all the tasks, but where each one will incur different costs to complete the distinct tasks due to machine specialization. This problem is presented as a cost matrix in Figure 12. The goal of the assignment problem is then to minimize the total cost required to complete the job without exceeding the available resources of the machines. So how does this apply to object tracking? The assignment problem in itself is an act of "linking." In the original context, it is to link a job to a machine. However, this can easily be deployed to link targets in consecutive image frames, or to merge two tracks into a more continuous single trajectory. The challenge in this case is that assignment can be performed in numerous possible ways and tracking algorithms will always provide an answer to the problem, so the issue is whether the answer provided is op-

timal. Assignment problem algorithms must therefore be based on a set of experimental parameters so that the subsequent answer is reproducible, quantifiable, and verifiable. This is where the cost matrix comes into play. In fact, the main feature that sets one tracking algorithm apart from another usually lies in the cost matrix, which will be explored further in the following sections.

Linear Assignment Problem Tracker

The linear assignment problem (LAP) is a widely used algorithm for object tracking (Jaqaman et al., 2008), and represents an approximation of the MHT approach. The LAP was originally devised to tackle two distinct sets of tracking needs: particle linking and subsequent track linking. Track linking is especially important in cases where targets undergo merging and/or splitting events as well as when particles potentially disappear for one or more frames only to be reacquired later. These complex decisions can be treated as individual "hypotheses," each in competition with the others. Each hypothesis can then be weighted by a cost function. For example, consider the costs of linking two particles:

Let C_{ij} be the cost of linking particles i and j, and d_{ij}^2 be the square of the distance between these particles.

Then, if d_{ij}^2 is greater than the maximum allowable distance set by the user, the cost l_{ij} is set to infinity, essential prohibiting the two particles from being linked.

Additional costs can be added to the cost matrix to handle other situations commonly

encountered in biological samples, taking into consideration such issues as whether the target maintains similar brightness from frame to frame, or whether the target maintains similar shape/size in consecutive frames. For example, one can add "features penalties" that would discourage linkage of particles that do not resemble one another. Accordingly, features can be preferentially weighted as follows:

$$p_{ij} = W \frac{|f_i - f_j|}{f_i + f_j} \quad \text{so that } C_{ij} = (d_{ij} \times p_{ij})^2,$$

where p_{ij} = cost of feature penalty, W = weighted factor, f_i = particle i feature (size, shape, etc.), and f_i = particle j feature (size, shape, etc.).

In treating each linking parameter that way, the LAP tracker associates every potential assignment with a cost, C. The LAP algorithm then identifies, in each step, the combination of assignments with the minimal sum of costs. The LAP algorithm as implemented by Jaqaman et al. (2008) works at two steps: (i) linking targets in consecutive frames, and (ii) linking tracks to form longer trajectories. In frame-to-frame linking, the decision must be made whether a target in frame t could be linked to another one in frame $t + 1$ (track continues) or linked to nothing (track ends). Conversely, a target in frame $t + 1$ may not be linked to one in frame t (track begins). The LAP tracker algorithm makes temporal decisions based on target relationships between consecutive frames, yet it makes decisions globally in space as it considers the global "cost" of making all the linkages. Therefore, while assignments with a lower cost are more likely to be selected, the requirement for a globally minimized cost could result in the selection of individual linkages in which the cost are not the lowest.

Kalman Filter

In addition to making decisions for target linking based on nearest neighbor or cost matrix algorithms, the accuracy of positional linking can be further enhanced based on predictions. This is powerful especially in the case where (i) the density of targets is high, leading to a high frequency of path-crossing incidents, and (ii) the targets move with roughly constant velocities, even though the velocity does not need to be the same for all the tracked targets. One predictive tool commonly used in motion tracking is the Kalman filter (Kalman, 1960; Smal, Draegestein, Galjart, Niessen, & Meijering, 2008). It is used to make predictions of future states based on past and present ones. When applied to motion tracking, the Kalman filter computes the most probable position of the target through the following steps as outlined in Figure 13: A nascent track of a moving target is created using the conventional cost-matrix-based LAP algorithm as discussed in the previous subsection. Each track created based on two consecutive positions of a target is now used to generate an instance of a Kalman filter (positions with dashed outlines in Fig. 13), which estimates the probable position of the target in the subsequent frame. Consequently, there will be as many Kalman filters as there are tracks. It is based on these "predicted" positions that the linking decisions are made, again, utilizing the LAP framework as the basic principle, with a user-defined square distance as the "cost."

As expected, Kalman filters enhance the accuracy of positional linking under conditions in which the density of targets to be tracked is high and particles move with a relatively constant velocity. Conversely, if the targets exhibit inconsistent velocities or rapid changes in direction, that will negatively impact the performance of the Kalman filters. The reason for this is that the Kalman filter assumes that target movement is not random. This highlights the fact that there are more complex types of movement behavior that need to be described. To achieve this, the data need to be mathematically modeled.

ANALYSIS AND MODELING OF TRACKING DATA

Ideally, the goal of any tracking experiment is to extract relevant, quantitative descriptors that provide meaningful biological information (Bannai, Lévi, Schweizer, Dahan, & Triller, 2006; Brandenburg & Zhuang, 2007; Goulian & Simon, 2000; Akihiro Kusumi et al., 2005; Monnier et al., 2015; Rothenberg et al., 2011; Ruthardt, Lamb, & Bräuchle, 2011; Seisenberger et al., 2001). In the case of SPT, such analyses will most often characterize particle motion, interaction, or both. Tracking of larger objects such as organelles or whole cells often encompass similar analyses, but with added complexities that may include changes in shape and intensity, as well as merging and/or splitting of multiple objects. This section will outline commonly used tracking analysis methods, with an eye towards both the underlying theoretical assumptions and practical considerations that should be taken into account, along with a key example from recent literature.
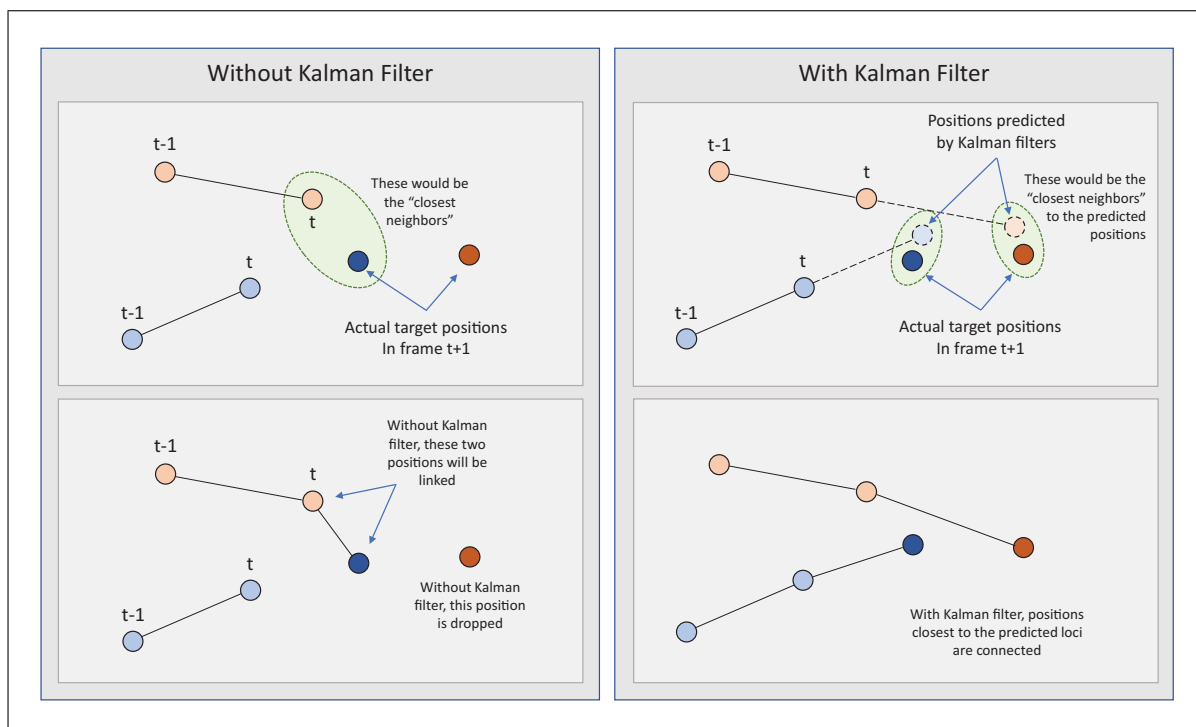
Figure 13 Kalman filter. At left, two nascent particle tracks are shown in light orange and light blue, respectively. Without using a Kalman approach, the light orange particle at time *t* is linked to the dark blue particle at time *t+1*, with the remaining dark orange particle unlinked. At right, the same nascent trajectories are shown. With the Kalman filter, the predicted changes in position of the light orange and light blue particles are found from time *t* to *t+1*. These predicted positions are then compared to the actual particle positions at *t+1*. In this way, position linking proceeds by extending both the orange and blue trajectories, on the basis of their prior behavior.

Measuring Particle Dynamics and Diffusion

Biomolecules move throughout a cell via a wide variety of means. Broadly speaking, these mechanisms can be classified as active, passive, or a mixture of both. Active transport of molecules or structures requires an energy source such as ATP and is often facilitated by molecular motors such as kinesin and myosin, among many others, in concert with a scaffold protein such as tubulin or actin. In such cases, it is useful to define the dynamic behavior of the particles via several parameters such as average velocity, instantaneous velocity, total distance traveled, and net distance traveled, among others. These quantities are easily calculated from the target trajectories developed in the steps described previously (Meijering, Dzyubachyk, & Smal, 2012).

Passive transport, on the other hand, is governed by the inherent diffusion of a molecule in whatever environment it is moving through, such as the cytoplasm, nucleus, or one of the many lipid membranes present in a cell. Diffusion can be described as a random motion of a particle that is solely determined by the exchange of kinetic energy between it and its surrounding molecules through collisions. Many biochemical processes are fundamentally limited by how quickly a molecule can diffuse to a region of interest; likewise, a disease state may manifest as aberrant diffusional behavior of one or more molecules (Trimble & Grinstein, 2015; Verkman, 2002). Thus, describing the diffusive behavior of a molecule in a cell can provide important insight.

Figure 14 broadly illustrates the various modes of transport that may be measured. In Figure 14A, a particle diffuses through a homogenous medium. Although the simplest scenario to characterize, this is rarely encountered in biological environments. In Figure 14B, a particle diffuses through a more biologically typical heterogenous medium, with temporally and/or spatially varying properties that affect particle diffusion. In Figure 14C, a particle diffuses in a more complex, heterogenous environment. Additional obstructions and/or energy sources can impede or potentiate the normal diffusion process, respectively. As can be surmised, quantifying diffusion can be more difficult than using the simpler distance and/or velocity metrics discussed above. This is because diffusion, unlike directed motion, is random in nature.
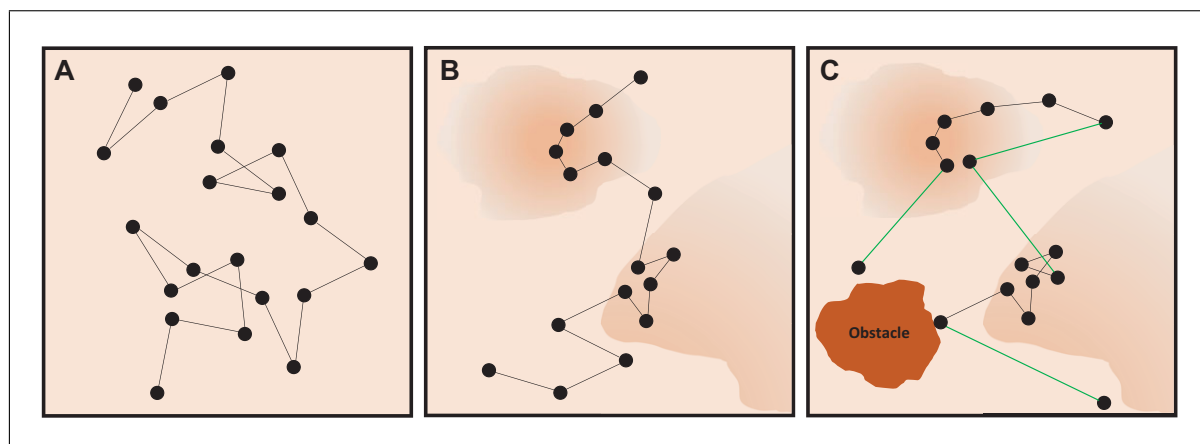
Figure 14 Particle movement through different diffusion environments. (**A**) Particle diffusion through a homogenous medium, which is rarely encountered in biological samples. (**B**) A more realistic scenario, in which a particle is diffusing through an environment with heterogeneous viscosity. (**C**) A more complex biological environment with heterogenous viscosity and obstructions, in which a particle moves via constrained and/or facilitated diffusion (green) resulting in stochastic and persistent movements, respectively.

An initial quantitative description of diffusion was proposed by Fick (Fick, 1855), in which he introduced the concept of a diffusion coefficient, usually denoted *D*. This parameter describes the mobility of a diffusing particle through some medium. Particles with high diffusion coefficients will tend to disperse in that medium more quickly than those with lower values. Fick showed that if one were to determine the overall distribution of a molecule at an initial time point, and then measured a change in its distribution over time, its diffusion coefficient could be determined.

This fact is exploited in various imaging methods such as fluorescence recovery after photobleaching (FRAP) and fluorescence loss in photobleaching (FLIP) (Lippincott-Schwartz & Patterson, 2003; Rabut & Ellenberg, 2004). But while widely utilized, FRAP and FLIP are inherently ensemble, or average, measurements. In other words, these methods do not easily discern local variations in diffusion, nor do they easily identify multiple diffusional states or particle subpopulations that may be critical to understanding a given biological behavior. To do so, it would be necessary to determine the diffusion coefficients for *individual molecules* across a range of locations and times in a sample.

SPT offers a way to measure this diffusion coefficients of individual particles within a sample. It is not an ensemble measurement method subject to the averaging effects of FRAP and FLIP; as such, it is better able to detect local spatiotemporal variations in diffusion or particle sub-populations with differing behaviors. To calculate the diffusion coefficient of a particle from its measured trajectory, it is important to distinguish between *distance* and *displacement*. The distance that a diffusing particle travels over any period of time is a scalar quantity. In other words, it will always be a positive value. Displacement, on the other hand, is a directional (or vector) quantity and can therefore be positive or negative. In the case of a freely diffusing particle, it has an equal chance of moving in any direction at any time point. So, while the total distance that a diffusing particle travels over any period of time is always positive, its net displacement, on average, is always zero (Berg, 1993).

However, the squared displacement of a particle will not be zero, since this quantity is always positive. In fact, the average (or mean) squared displacement of a particle over a given time interval provides the key to calculating its diffusion coefficient. It has been shown that in an ideal situation, whereby a particle is randomly and isotropically diffusing, the following relationship exists (Chandrasekhar, 1943):

$$\text{MSD} = 2\gamma D \Delta t.$$

Here, MSD is the *mean squared displacement* and Δt represents a time interval. To better understand this relationship, consider a particle that was imaged for 100 s in 1-s increments (101 frames). The possible values of Δt to consider are then 1, 2, 3, and so on up to 100 s. The MSDs are calculated for each possible time interval. Thus, for a single particle trajectory, 100 displacements can be calculated for $\Delta t = 1$ s, such that these displacements are then squared and subsequently averaged to get an MSD value. Likewise, 50
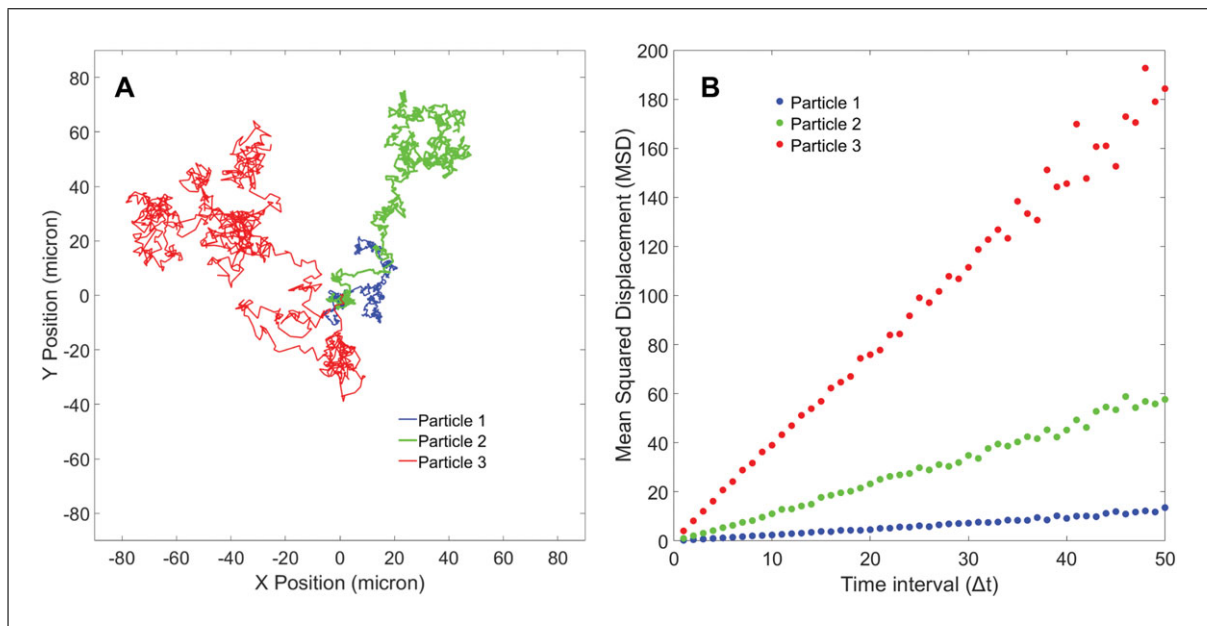
Figure 15 MSD analysis for freely diffusing particles. In (**A**), three example particle trajectories are shown in blue, green, and red, respectively. Each particle starts at the origin (0,0) and diffuses randomly in the *x* and *y* directions over time. In (**B**), the MSD as a function of Δt is plotted for each particle. Note that in this case, each particle exhibits a linear MSD vs. Δt relationship, but with each having a different slope. This would indicate different diffusion coefficients for each particle.

displacements can be calculated for each 2-s interval, and so on. The above equation indicates that the MSD of a particle is a linear function of the time interval being considered. The slope of that line is $2\gamma D$, where γ indicates the number of spatial dimensions through which the particle can diffuse.

It is important to consider the value of γ in light of the biological behavior being measured. For example, if a molecule is randomly diffusing in a membrane, $\gamma = 2$, since the particle can only move within the 2D plane of the lipid bilayer. Conversely, if a molecule is diffusing throughout the cytoplasm or nucleus, it is free to diffuse in three directions, making 3 the appropriate value for γ. In either case, computing the slope of the MSD of a particle vs. Δt curve via a least-squares regression can yield the diffusion coefficient (*D*) of an individual particle. Furthermore, it requires no prior knowledge of its properties or surroundings, save its positions over time and the number of degrees of freedom of its motion, as illustrated in Figure 15. In Figure 15A, three 2D particle trajectories are shown in red, green, and blue, respectively. In Figure 15B, the color-corresponding MSD vs. Δt curves are shown for each particle, with a linear relationship evident. Since the three plots have markedly different slopes, it is surmised that the three particles have different diffusion coefficients.

Practical Considerations

As discussed above, MSD values can be calculated for any Δt that is less than the duration of the particle trajectory. However, as Δt increases, the number of displacements that are averaged to calculate the MSD decreases. For example, again consider a particle trajectory lasting 100 s, captured at 1-s intervals. For $\Delta t = 1$ s, 100 independent displacements can be calculated. However, only one displacement value exists for $\Delta t = 100$ s. Thus, the MSD value for $\Delta t = 1$ s is expected to be much better averaged than the value for $\Delta t = 100$ s. In general, the larger the Δt value (relative to the total trajectory length), the more statistical fluctuation there will be in the MSD value. This can very often result in MSD vs. Δt curves that diverge widely from the linear case for large Δt. For that reason, it is advisable to only consider a portion of the total possible MSD vs. Δt curve to calculate a diffusion coefficient. Michalet provides an excellent and in-depth exploration of the optimal number of Δt values to include in the least-squares fit (Michalet & Berglund, 2012; Qian, Sheetz, & Elson, 1991). However, many algorithms, in practice, simply compute the diffusion coefficient using the first 10% to 25% of Δt values, while ignoring the remainder.

A second practical factor to consider is localization error. As discussed previously, the ability to accurately determine the location of

a particle depends on its brightness, its speed, and the exposure time of the camera used to record the image. As a simple approximation, the equation above is modified to account for the localization uncertainty (Michalet, 2010):

$$\text{MSD} = 2\gamma D\Delta t + 2\gamma\sigma^2.$$

Here, σ is the localization uncertainty with the other parameters already defined. Thus, we can see that the particle localization error will create a positive offset in an MSD curve, which can be extracted from least-squares regression. We refer readers to other studies (Berglund, 2010; Gal, Lechtman-Goldstein, & Weihs, 2013; Michalet, 2010; Michalet & Berglund, 2012; Saxton, 1997; Saxton, 2009) for more in-depth exploration of optimal MSD curve analysis.

Measuring Non-ideal Diffusion

A hallmark of "ideal" diffusion — also called *Fickian* or *Brownian motion* — is that a particle is equally likely to move in the positive or negative direction at all points along its trajectory. This may be true even in heterogeneous environments, as illustrated in Figure 14A and B. However, we can imagine that this is very often not the case in complex biological systems. Molecules may be "confined" in one or more dimensions by rigid structures within membranes or the cytoplasm (Kusumi, Sako, & Yamamoto, 1993; Saxton, 1995; Saxton & Jacobson, 1997; Schütz, Schindler, & Schmidt, 1997). Conversely, molecules may often undergo directed motion potentiated by an external energy source such as ATP (Saxton, 1994), as shown in Figure 14C. Either of these situations may result in so-called *anomalous diffusion*, whereby linear MSD analysis does not hold well.

Consider again Figure 15. Although each particle displays a unique MSD vs. Δt curve, the corresponding slopes are linear. In other words, the MSD of a particle per time lag does not change throughout the length of its trajectory. Conversely, consider a particle diffusing through an actin meshwork. At small time scales, the particle may behave as a freely diffusing molecule. But, at larger time scales, the particle will eventually encounter an actin filament that serves to restrict its motion. In such cases, the slope of the MSD curve might not be constant but could decrease with larger Δt values. This is referred to as *sub-diffusion*. Likewise, an increase in the slope of the MSD curve with larger Δt values may indicate the opposite; the squared displacements become bigger than expected at longer time intervals, indicating that some additional energy source is being expended to move the particle over longer time scales. Such behavior is often termed *super-diffusion*, or facilitated/active transport, and is indicative of some external force acting on a particle beyond its natural diffusive behavior. To account for such non-linear behavior (anomalous diffusion), a multitude of models have been proposed. The approach that has been most extensively employed uses the power-law formulation (Metzler & Klafter, 2000; Metzler, Jeon, Cherstvy, & Barkai, 2014; Saxton, 1997):

$$\text{MSD} = 2\gamma D\Delta t^\alpha.$$

As can be seen, this formulation adds an additional parameter α to the relationship between MSD and Δt. To help understand the meaning of the α value, Figure 16A, B, and C illustrate the behaviors described previously. In panel A, a particle is allowed to diffuse freely, albeit through a heterogeneous medium. In B and C, a particle encounters obstructions to free diffusion and external energy sources, respectively, that cause its motion to deviate from ideal diffusion. Figure 16D illustrates the effect of different values of α on the MSD curve. With an α value near 1, the curve remains linear and can thus be thought of as reflecting ideal Brownian motion (blue curve). Values less than 1 indicate confined or sub-diffusion (green curve). Likewise, α values greater than 1 suggest facilitated or super-diffusion. While particle tracking data can be modeled using the above equation, it is generally more convenient to use a log-log form to extract D and α values:

$$\log(\text{MSD}) = \alpha \log(\Delta t) + \log(2\gamma D).$$

In this way, the regression is now linear, with the slope equal to α, such that the y intercept can be used to determine the diffusion coefficient, as shown in Figure 16E.

Using a power-law relationship to measure anomalous diffusion provides a simple yet powerful way to draw important biological conclusions. In addition to providing a simple means to determine the diffusion coefficient, the MSD curve has the useful property that non-linearity of the curve can give convincing evidence of suppressed or facilitated dynamic behavior, thereby implying potential interactions between the molecules of interest and other structures.

The power-law formulation can be extremely useful in determining to what extent particles undergo "non-ideal" diffusion. However, other analyses can give complementary
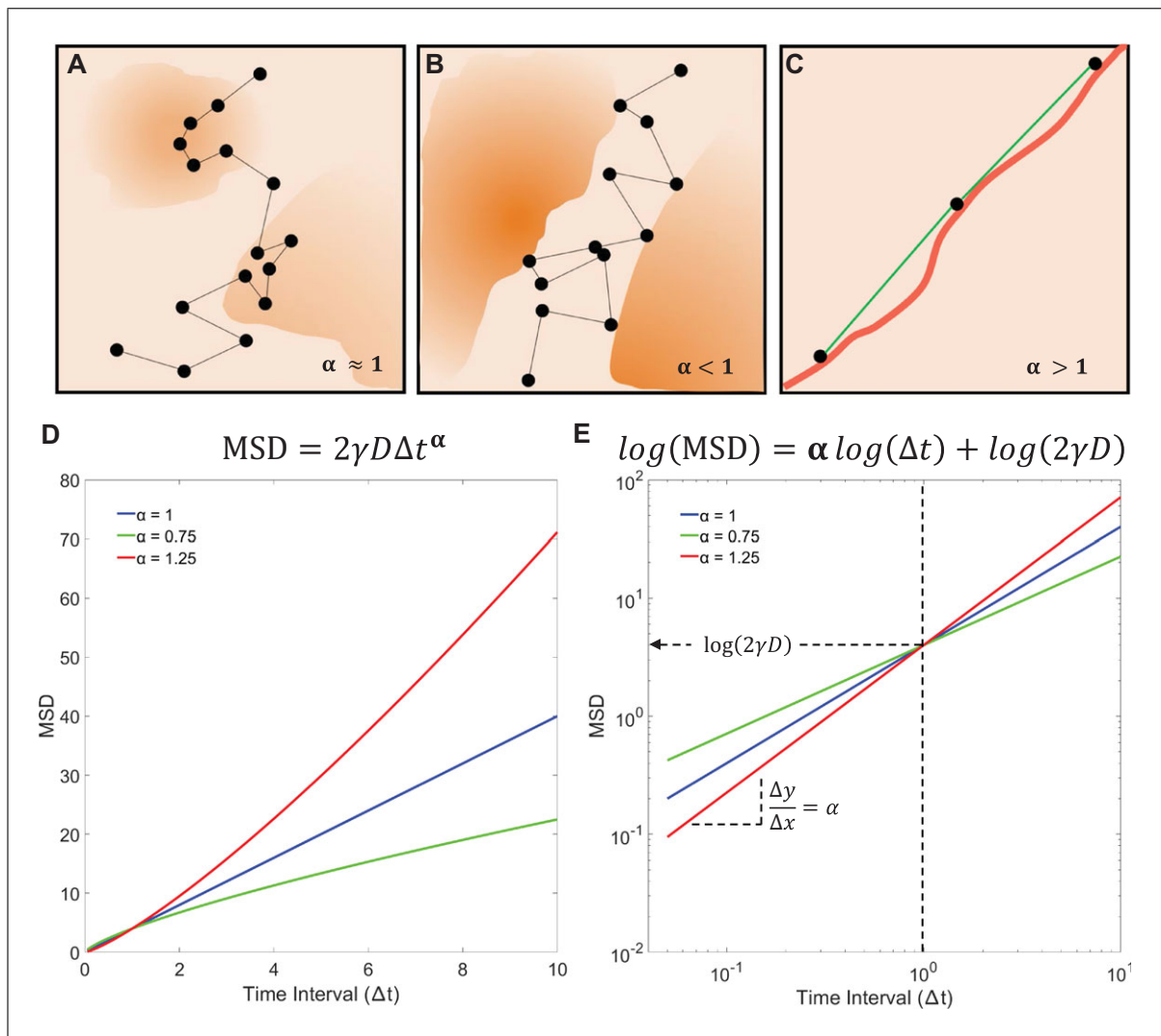
Figure 16 MSD analysis for particles undergoing different diffusive behaviors. (**A**, **B**, and **C**) Illustrations for a particle exhibiting simple Brownian motion, constrained or sub-diffusion motion, and facilitated or super-diffusion motion, respectively. (**D**) MSD vs. Δt curves showing the effect of different values for α. (**E**) The same data but plotted in log-log format. This transformation linearizes the relationship, making the extraction of α and D values mathematically simpler.

information. MSD analysis simply considers the displacements of a particle; missing is any characterization of particle direction. To that end, the tendency of a particle to change direction between time points can also be quantified (Wilson et al., 2016), as shown in Figure 17.

In Figure 17A, each of the particles has the same average displacement magnitude per time point, yet their trajectories look markedly different. Calculating the change in direction (represented by an angle) between each successive time point in the trajectories generates the circular histograms shown in Figure B, C, and D, also called rose plots. The change in direction (angle) of a particle is represented along the azimuthal axis, while the frequency for that angle range is displayed along the radial direction. Note that for the blue trajec-

tory, the particle shows a near-equal chance of changing direction from one time point to the next. This would indicate Brownian, or random, motion. But for the green trajectory, the particle tends to continue along the same direction, and thus the rose plot is centered around 0°. This behavior can be seen in many scenarios, such as cargo transport along microtubules. Conversely, the red trajectory tends to reverse direction at each successive time point, as shown by a rose plot centered near 180°. As can be imagined, this may be seen in situations where a particle's motion is constrained — this may indicate some trapping mechanism (such as a cargo molecule stuck inside a vesicle) or may suggest a binding event. For example, a signaling subunit binding to an engaged membrane receptor may display confined diffusion
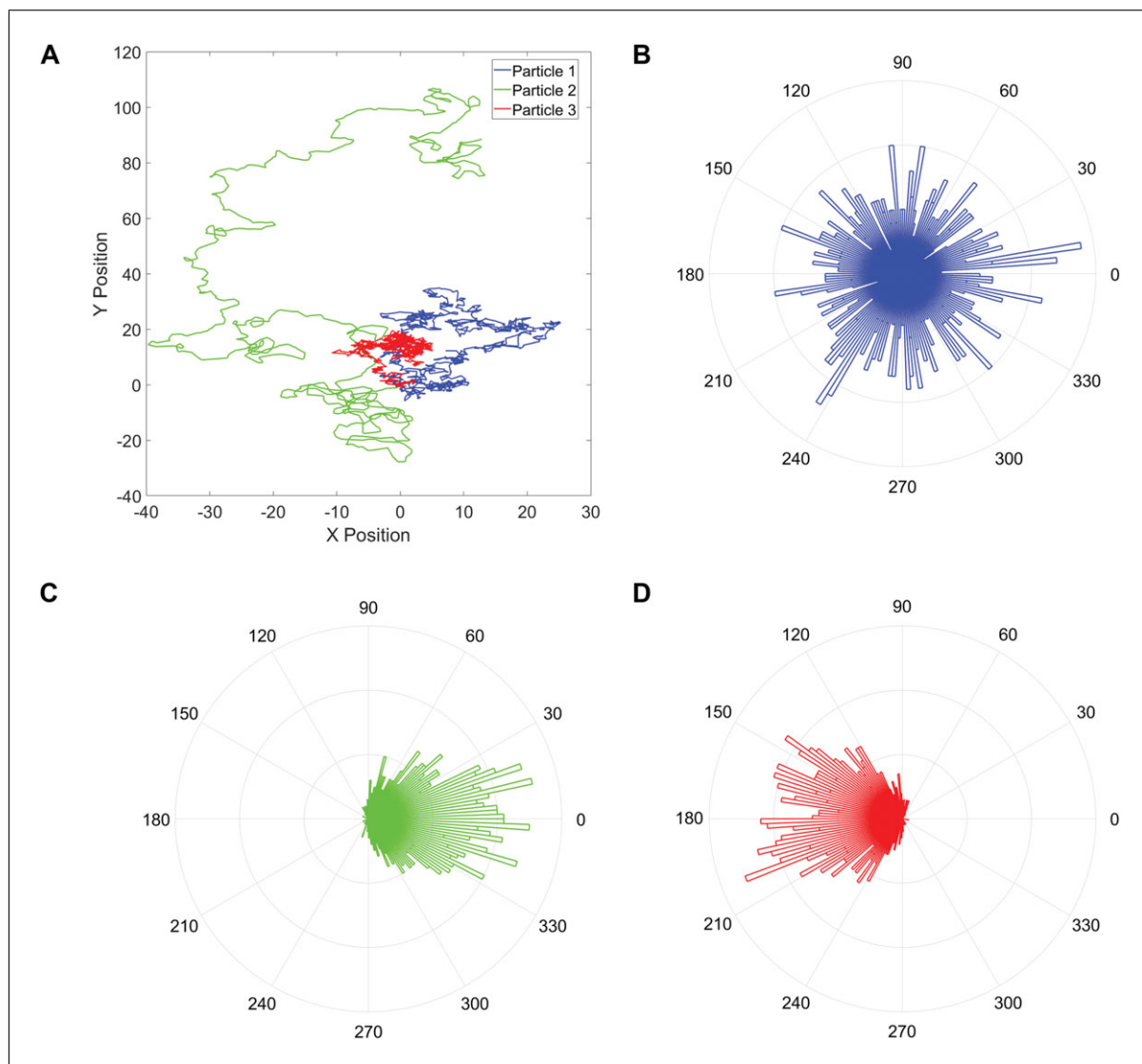
Aaron et al.

Figure 17 Particle persistence direction and non-ideal diffusion. In (**A**), three particle trajectories are shown in blue, green, and red. Calculating the change in direction of each particle across all time points makes it possible to plot radial histograms (also called rose plots) in (B, C, and D). In these plots, the change in direction per time point is represented as an angle, plotted in the azimuthal direction. The relative frequency of those changes is indicated by the radial length of each bar. (**B**) Note that the blue particle does not display a strong preference in its change in direction — the histogram is roughly "circular," indicative of random, Brownian motion. (**C**) The green particle, on the other hand, tends to change relatively little in its direction, and thus its radial histogram is centered near 0°. This is suggestive of facilitated diffusion. (**D**) The red particle, in contrast, tends to move in the opposite direction from each successive time point, as evidenced by a directional histogram centered at near 180°. This suggests confined diffusion, as the particle changes direction more often than would be seen under random diffusion conditions.

because its native diffusion is hampered by its interaction with the receptor.

Multiple State Modeling

The above analysis methods implicitly assume that the diffusion coefficient of a given particle, calculated from a single trajectory (or portion thereof), is constant. However, a number of biological processes do not follow this assumption. For example, it has been suggested that transcription factors find their cognate binding sites via a "search" mechanism involving saltatory movement. In other words, these molecules can be thought of as having "fast" and "slow" diffusional states. Conventional MSD analysis would paint an incomplete picture of this heterogenous mobility, as by definition, it represents an averaging of particle displacements throughout its trajectory. Several techniques have been developed to characterize various diffusive movements by isolating these states, within a single trajectory, and studying them independently, such as through transient confinement
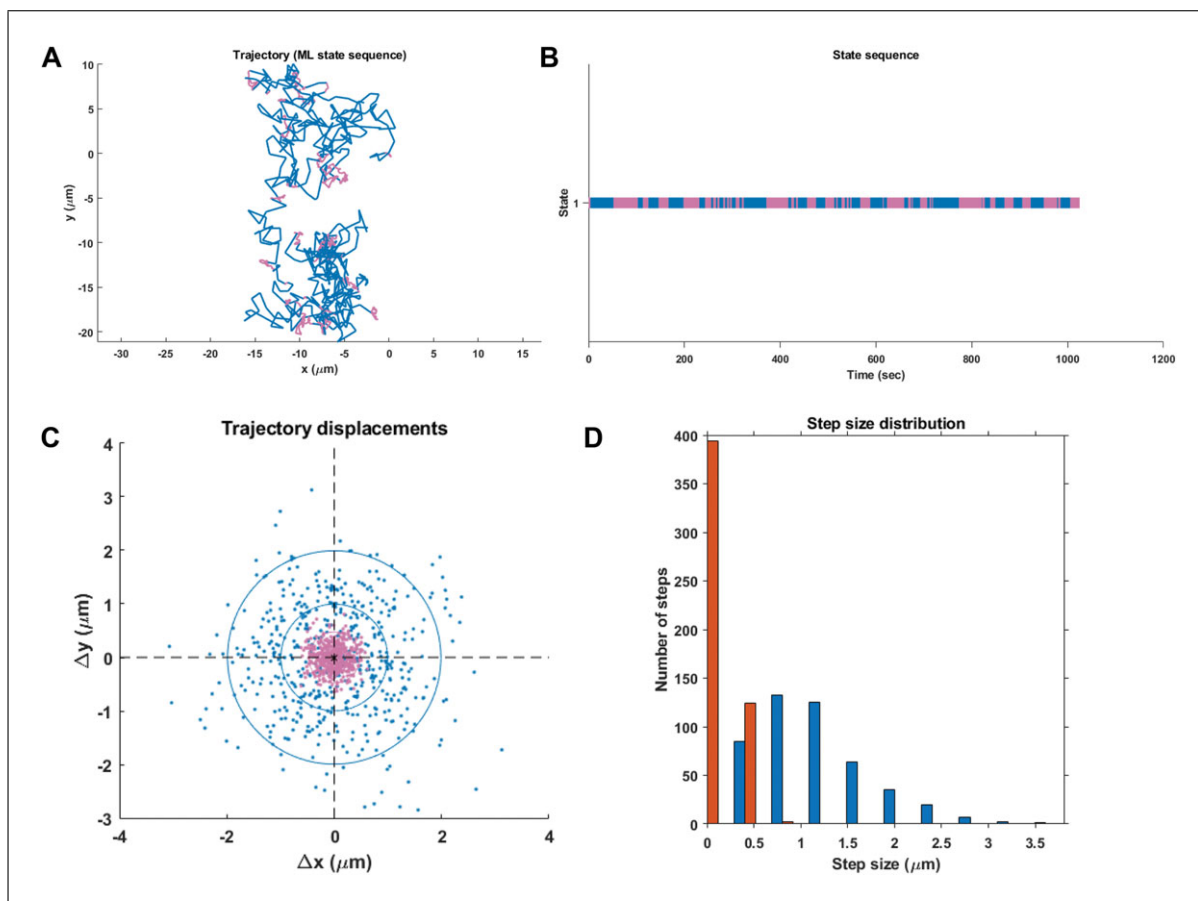
Figure 18 Bayesian selection of hidden Markov modeling (HMM-Bayes) analysis of multistate particle diffusion. In (**A**), a single particle trajectory is shown, with segments corresponding to "slow" diffusion in pink and to "fast" diffusion in blue. In (**B**), diffusional state changes and duration are indicated as segments across the length of the trajectory. In (**C**), a scatter plot shows per-frame displacements. Note the slow displacements (pink) are clustered nearer zero than the fast displacements (blue). In (**D**), a histogram of displacement values is shown, with a clear separation between slow and fast states.

zone analysis (Simson, Sheets, & Jacobson, 1995).

A recently reported method by Monnier et al., termed HMM-Bayes, offers a Bayesian statistical approach to extract multiple diffusion coefficients from a single particle trajectory via hidden Markov modeling (Monnier et al., 2015). While the approach requires users to specify the maximum number of diffusional (or active transport) states that a particle can exhibit, it proposes the simplest model to explain a given trajectory. An example analysis is shown in Figure 18A for a single-particle trajectory exhibiting multi-state diffusion. After analysis using the HMM-Bayes algorithm, each segment in the trajectory is assigned to either a "fast" or a "slow" diffusional state, denoted by blue and pink, respectively. Figure 18B illustrates the amount of time the particle spends in each diffusional state as segments of the trajectory length. Figure 18C and D show a scatter plot of *x/y* displacements (with the same color scheme) and a histogram of displacement magnitudes, respectively.

As can be seen, there are a multitude of factors that need to be considered when attempting to characterize particle diffusion in cells. SPT offers the unique capability of measuring molecular motion on a per-particle basis, thereby avoiding artifacts due to ensemble averaging. However, researchers should approach such analyses with caution. MSD analysis should be done with knowledge of (i) the localization uncertainty inherent in the data and (ii) the appropriate number of time lags in order to give an accurate measure of diffusion coefficients. Researchers should also assess the degree to which particle behavior deviates from ideal Brownian motion. Tools such as those described in Figure 17 can aid in determining whether anomalous diffusion models, such as a power-law formulation, will be a more appropriate choice. Furthermore, researchers should consider whether the
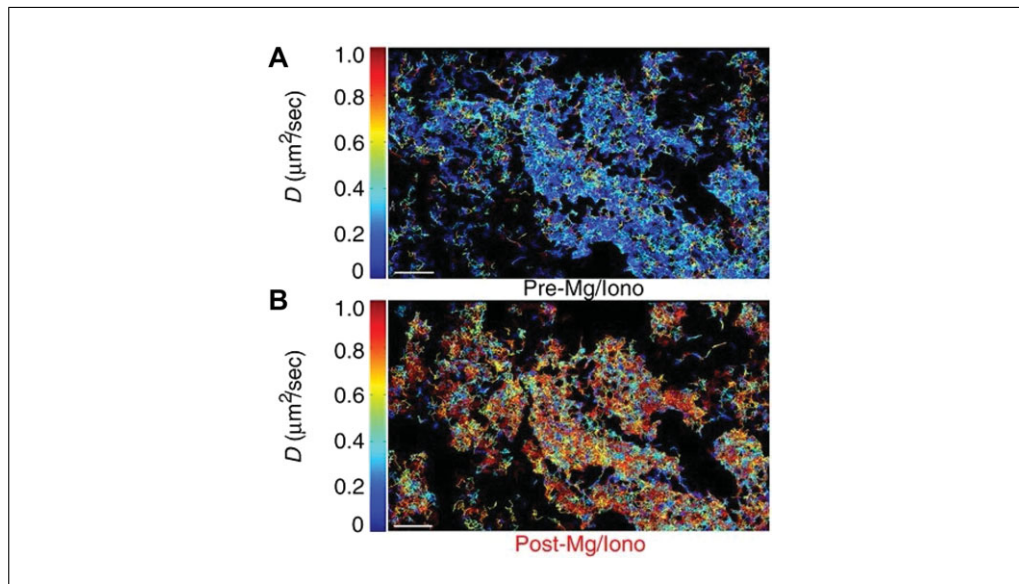
Figure 19 Plots of several thousand single-molecule trajectories in HEK293T cells expressing a halo-tagged rhomboid-like 2 (RHBDL2) protein in the plasma membrane. The trajectories were plotted such that the line color corresponds to the modeling diffusion coefficient, as indicated by the color bar to the left of each plot. In (**A**), trajectories are shown for a group of cells in normal medium. In (**B**), SPT results are shown for the same cells after addition of Mg-ionomycin. The color-encoded diffusion constants show a clear increase in the overall diffusivity of RHBDL2. These results correlated well with an increase in the protein's enzymatic activity, providing novel insight into its cellular function. This method of trajectory visualization can also be used to identify areas of relative high and low particle diffusion. Results adapted with permission from Kreutzberger et al. (2019).

molecules of interest may be displaying saltatory motion — in which case, it is advisable to attempt extracting multiple motion descriptors from a given particle track.

Taking these considerations together, single-particle tracking can be a powerful method to generate novel biological insights. For example, Urban and colleagues recently used SPT-TIRF microscopy to show surprisingly unique dynamic behavior of membrane-bound rhomboid proteins in several cell types (Kreutzberger, Ji, Aaron, Mihaljević, & Urban, 2019). This example illustrates many of the aspects discussed above. Firstly, fluorophore and instrument selection were optimized prior to data acquisition. Halo-conjugated Janelia Fluor dyes were used in this case because of their superior brightness and photostability (Grimm et al., 2015), as well as genetic specificity. TIRF microscopy was chosen as the ideal imaging modality, as it pairs high imaging speed with excellent background rejection for imaging events near the plasma membrane. Once data were collected, aforementioned imaging processing techniques were used, including background subtraction and Gaussian denoising. Subsequently, particles were detected via threshold application, localized via Gaussian fitting, and positions liked via nearest-neighbor analysis to form trajectories using the Mosaic particle tracking plugin for ImageJ (Sbalzarini & Koumoutsakos, 2005), one of a number of freely available tracking algorithms (Meijering et al., 2012).

Figure 19 (adapted with permission from Kreutzberger et al., 2019) shows HEK293T cells transfected with N-Halo-tagged rhomboid-like 2 (RHBDL2) proteins, and labeled with Janelia Fluor 549 dye. In Figure 19A, cells were first imaged in normal imaging medium; Figure 19B shows the same field of view after treatment with Mg^{2+} and ionomycin. In both cases, single molecules were tracked, and diffusion constants (D) were extracted as outlined above for each particle trajectory. Trajectories were then drawn using a color scheme that indicates each respective value of D. As suggested by the images, average diffusion constants increased by 2.5-fold after this treatment. Interestingly, this correlated very well with an increase in enzymatic activity, thereby clearly relating rhomboid diffusion to its function. The color-encoded representation here can also be very useful in visualizing changes in diffusion behavior in

specific locations of a cell or tissue, thereby identifying local areas of relative high or low diffusion.

Object Tracking: Cell Dynamics and Lineage Mapping

The discussion thus far has concentrated on the tracking of *particles*, which can be treated as point-like sources. As such, determining particle position over time is generally sufficient to accomplish most common analyses such as diffusivity measurements. However, tracking analysis can involve *objects* as well. Many of the same analyses presented above can be applied to tracking larger objects. However, diffusion-based metrics may not be as useful in the case of organelles and cells. Rather, parameters such as velocity (both average and instantaneous) and distance traveled, among others, may be more informative (Meijering et al., 2012; Meijering et al., 2006). Furthermore, object tracking also affords the ability to analyze morphological parameters. Simple metrics such as surface area, volume, and eccentricity, as well as convexity and concavity, can be useful in describing dynamic cell behavior in the context of tracking. More complex shape descriptors such as those based on Zernike polynomials or principal-component analysis have also been shown to be useful (Pincus & Theriot, 2007).

Cellular dynamics combined with lineage-mapping methods are highly prevalent in developmental biology. In this context, lineage mapping refers to the tracking of both cell position and cell division into progeny within the developmental stage of a living organism. While canonical cell lineage mapping has been determined for simpler organisms such as *Caenorhabiditis elegans*, modern lineage mapping is nevertheless an active field of research for more complex organisms as well as for the analysis of mutant phenotypes and other more in-depth investigations (Amat et al., 2014; Chalfoun et al., 2016; Christensen et al., 2015; Heid, Voss, & Soll, 2002; McDole et al., 2018; Sato, Rancourt, Sato, & Satoh, 2016; Stegmaier et al., 2016; Tassy, Daian, Hudson, Bertrand, & Lemaire, 2006; Winter et al., 2011).

As a state-of-the-art example, a comprehensive exploration of mouse embryogenesis using multi-view light-sheet microscopy in tandem with novel computational frameworks has been reported (McDole et al., 2018). In this expansive study, advanced cell tracking was performed under several scenarios using a modular set of computational tools that are all publicly available. Initial cell identification and tracking was performed using a Gaussian mixture model (Amat et al., 2014) supplemented with a machine-learning component, referred to as TGMM v2.0. Although this approach can identify cell divisions, a separate convolutional neural network approach was implemented to detect mitosis events with higher accuracy.

In Figure 20, results from an example cell-tracking experiment are shown, describing the dynamics of epiblast cells as they traverse and exit the primitive streak. McDole and colleagues reconstructed lineages of individual epiblast cells traversing the primitive streak using a mosaic reporting approach (Pontes-Quero et al., 2017), whereby only a subset of cells express a fluorescent reporter. In Figure 20A, tracks are shown of cells that enter the streak and exit on the opposite side. In Figure 20B, tracks are shown of cells that enter the streak and divide, and whose daughter cells exit the opposite side. In Figure 20C, cell lineage tree diagrams show the proliferative behavior of the cells described in the previous panels. The black lineage tree indicates cells that entered the primitive streak but did not exit the opposite side. Cell lineage diagrams, such as this one, typically represent time along one direction and bifurcations in each line indicate cell division events, such that the progenitor of each cell can be identified.

This example highlights the wealth of biologically relevant information — both dynamic and morphological — that can be available when performing object tracking. Ultimately, the appropriate summary statistics that adequately describe a tracking experiment will depend entirely on the biological question at hand. However, the potential for measurement bias is nearly always present. While innovative ways to remove such biases has received attention (Zaritsky et al., 2017), often the most meaningful conclusions in any tracking experiment are those based on comparisons between samples, conditions, or other perturbations rather than on the absolute value of any particular parameter.

FUTURE DEVELOPMENT

As our ability to acquire increasingly more complicated live-cell imaging data advances with modern technologies, so does the importance of particle- and object-tracking analysis. Applied appropriately, these analyses can reveal subtleties of movement unnoticeable to the human eye. Yet, as has been shown by direct comparison (Chenouard et al., 2014), as
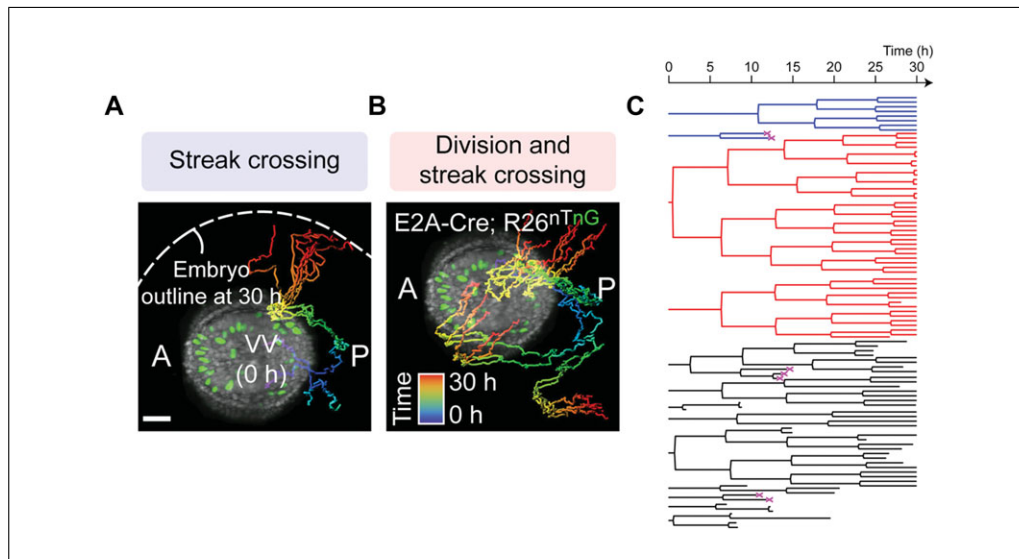
Figure 20 Epiblast cell tracing in developing mouse embryo. In (**A**), tracks are shown of cells that enter the primitive streak and exit at opposite sides. In (**B**), tracks are shown of cells that enter and divide, and whose daughter cells exit through opposite sides. In (**C**), cell lineage trees are shown for the cells represented in (A) and (B). Note that the horizontal direction indicates time, with bifurcations in the traces denoting cell division events. Blue traces indicate cells that behaved like those indicated in (A); red traces indicate cells that behaved like those described in (B); and black traces indicate cells that traversed the primitive streak but did not exit on the opposite side. A pink "X" denotes apparent cell death.

well as explained here, there is currently no universally applicable best approach. In this guide, we aim to balance the breadth of the various steps and challenges involved in performing a successful tracking analysis with the depth of knowledge required to gain basic understanding of the underlying principles of each method — from image acquisition to subsequent measurements.

The deluge of data created by the next generation of microscopes will challenge the current state of the art for annotating, standardizing, storing, compressing, processing, and analyzing multi-dimensional imaging data (Amat et al., 2015; Meijering et al., 2006). More importantly, the prospect highlights several challenges currently facing tracking analysis. (i) For example, none of the tracking strategies covered in this paper deals with the difficult challenge of tracking targets of interest in the context of a moving organism. Yet, the recent advances in light-sheet microscopes (Huisken & Stainier, 2009; Huisken, Swoger, Del Bene, Wittbrodt, & Stelzer, 2004; Ji, Shroff, Zhong, & Betzig, 2008; McDole et al., 2018; Vladimirov et al., 2014) are tailored specifically to address this type of biological question. Several recent innovative approaches (Christensen et al., 2015; McDole et al., 2018) provide exciting examples of how tracking and lineaging algorithms can be

adapted to these systemic biological questions in the future. (ii) Our paper focuses on tracking targets that can be easily segmented from high-SNR images or after successful image processing. However, there are structures in biology for which this may not hold true. Examples are nebulous molecular clouds such as ionic signaling waves, fluidic flow or turbulences, and the movement of macromolecular network. These are "structures" that cannot be easily segmented, yet their movements may have significant biological implications; application of novel mathematics and algorithms would be required before their movements could be measured. (iii) The present practice of treating image acquisition and data analysis as distinct, independent steps may soon no longer be a practical option. In fact, it is of utmost importance to unite microscope design, image file architecture, metadata standardization, and computational techniques into a seamlessly integrated strategy (Amat et al., 2014).

The pace of image data generation has thus far exceeded the development of analytical algorithms and the processing capabilities of most labs. The complexity of biological information will also limit how widely applicable many of the newly developed algorithms could be, given that they are usually driven by focused hypotheses and labeling of specific biostructures. This challenge therefore

highlights the importance of adaptive data analysis and of the use of machine-learning approaches. The interdisciplinary dialogue between biologists and data scientists is still lagging in regard to how to turn seemingly complex biological questions into tractable analytical problems. Future development of sophisticated tracking algorithms, especially if human supervision is to be minimized, will require biologists to be proficient enough in the basic principles of image analysis to articulate the questions in unambiguous and non-anecdotal terms. Even machine learning methods will inevitably require the informed optimization of parameters based on *a priori* knowledge to successfully execute computational image analysis.

LITERATURE CITED

Abrahamsson, S., Chen, J., Hajj, B., Stallinga, S., Katsov, A. Y., Wisniewski, J., ... Gustafsson, M. G. L. (2013). Fast multicolor 3D imaging using aberration-corrected multifocus microscopy. *Nature Methods*, *10*(1), 60–63. doi: 10.1038/nmeth.2277.

Amat, F., Höckendorf, B., Wan, Y., Lemon, W. C., McDole, K., & Keller, P. J. (2015). Efficient processing and analysis of large-scale light-sheet microscopy data. *Nature Protocols*, *10*, 1679–1696. doi: 10.1038/nprot.2015.111.

Amat, F., Lemon, W., Mossing, D. P., McDole, K., Wan, Y., Branson, K., ... Keller, P. J. (2014). Fast, accurate reconstruction of cell lineages from large-scale fluorescence microscopy data. *Nature Methods*, *11*, 951–958. doi: 10.1038/nmeth.3036.

Ayers, G. R., & Dainty, J. C. (1988). Iterative blind deconvolution method and its applications. *Optics Letters*, *13*(7), 547–549. doi: 10.1364/OL.13.000547.

Bajcsy, P., Cardone, A., Chalfoun, J., Halter, M., Juba, D., Kociolek, M., ... Brady, M. (2015). Survey statistics of automated segmentations applied to optical imaging of mammalian cells. *BMC Bioinformatics*, *16*(1), 330. doi: 10.1186/s12859-015-0762-2.

Balzarotti, F., Eilers, Y., Gwosch, K. C., Gynna, A. H., Westphal, V., Stefani, F. D., ... Hell, S. W. (2017). Nanometer resolution imaging and tracking of fluorescent molecules with minimal photon fluxes. *Science*, *355*(6325), 606–612. doi: 10.1126/science.aak9913.

Bannai, H., Lévi, S., Schweizer, C., Dahan, M., & Triller, A. (2006). Imaging the lateral diffusion of membrane molecules with quantum dots. *Nature Protocols*, *1*(6), 2628–2634. doi: 10.1038/nprot.2006.429.

Berg, H. (1993). *Random walks in biology: Expanded edition*. Princeton, N.J.: Princeton University Press.

Berglund, A. J. (2010). Statistics of camera-based single-particle tracking. *Physical Review E*, *82*, 011917. doi: 10.1103/PhysRevE.82.011917.

Beucher, S., & Lantuejoul, C. (1979). Use of watersheds in contour detection. *Proceedings of the International Workshop on Image Processing: Real-Time Edge and Motion Detection/Estimation, Rennes, 1979*.

Birch, P., Mitra, B., Bangalore, N. M., Rehman, S., Young, R., & Chatwin, C. (2010). Approximate bandpass and frequency response models of the difference of Gaussian filter. *Optics Communications*, *283*(24), 4942–4948. doi: 10.1016/j.optcom.2010.07.047.

Bobroff, N. (1998). Position measurement with a resolution and noise-limited instrument. *Review of Scientific Instruments*, *57*(6), 1152–1157. doi: 10.1063/1.1138619.

Brandenburg, B., & Zhuang, X. (2007). Virus trafficking—learning from single-virus tracking. *Nature Reviews Microbiology*, *5*(3), 197–208. doi: 10.1038/nrmicro1615.

Buades, A., Coll, B., & Morel, J. (2005). A non-local algorithm for image denoising. *Proceedings of the 2005 IEEE Computer Society Conference on Computer Vision and Pattern Recognition (CVPR '05)*, *2*, 60–61.

Calebiro, D., Rieken, F., Wagner, J., Sungkaworn, T., Zabel, U., Borzi, A., ... Lohse, M. J. (2013). Single-molecule analysis of fluorescently labeled G-protein–coupled receptors reveals complexes with distinct dynamics and organization. *Proceedings of the National Academy of Sciences*, *110*(2), 743–748. doi: 10.1073/pnas.1205798110.

Carter, B. C., Shubeita, G. T., & Gross, S. P. (2005). Tracking single particles: A user-friendly quantitative evaluation. *Physical Biology*, *2*(1), 60–72. doi: 10.1088/1478-3967/2/1/008.

Chalfoun, J., Majurski, M., Dima, A., Halter, M., Bhadriraju, K., & Brady, M. (2016). Lineage mapper: A versatile cell and particle tracker. *Scientific Reports*, *6*(36984), 1–9. doi: 10.1038/srep36984.

Chandrasekhar, S. (1943). Stochastic problems in physics and astronomy. *Reviews of Modern Physics*, *15*(1), 1–89. doi: 10.1103/RevModPhys.15.1.

Chen, B. C., Legant, W. R., Wang, K., Shao, L., Milkie, D. E., Davidson, M. W., ... Betzig, E. (2014). Lattice light-sheet microscopy: Imaging molecules to embryos at high spatiotemporal resolution. *Science*, *346*(6208), 1257998. doi: 10.1126/science.1257998.

Chenouard, N., Bloch, I., & Olivo-Marin, J. C. (2013). Multiple hypothesis tracking for cluttered biological image sequences. *IEEE Transactions on Pattern Analysis and Machine Intelligence*, *35*(11), 2736–2750. doi: 10.1109/TPAMI.2013.97.

Chenouard, N., Smal, I., De Chaumont, F., Maška, M., Sbalzarini, I. F., Gong, Y., ... Meijering, E.

(2014). Objective comparison of particle tracking methods. *Nature Methods*, *11*(3), 281–289. doi: 10.1038/nmeth.2808.

Christensen, R. P., Bokinsky, A., Santella, A., Wu, Y., Marquina-Solis, J., Guo, M., . . . Tashakkori, N. (2015). Untwisting the *Caenorhabditis elegans* embryo. *Elife*, *4*, e10070. doi: 10.7554/eLife.10070.

Crocker, J. C., & Grier, D. G. (1996). Methods of digital video microscopy for colloidal studies. *Journal of Colloid and Interface Science*, *179*, 298–310. doi: 10.1006/jcis.1996.0217.

Dean, K. M., & Palmer, A. E. (2014). Advances in fluorescence labeling strategies for dynamic cellular imaging. *Nature Chemical Biology*, *10*(7), 512–523. doi: 10.1038/nchembio.1556.

Denninger, P., Bleckmann, A., Lausser, A., Vogler, F., Ott, T., Ehrhardt, D. W., . . . Grossmann, G. (2014). Male–female communication triggers calcium signatures during fertilization in Arabidopsis. *Nature Communications*, *5*, 4645. doi: 10.1038/ncomms5645.

DeSantis, M. C., Zareh, S. K., Li, X., Blankenship, R. E., & Wang, Y. M. (2012). Single-image axial localization precision analysis for individual fluorophores. *Optics Express*, *20*(3), 3057–3065. doi: 10.1364/OE.20.003057.

Deschout, H., Zanacchi, F. C., Mlodzianoski, M., Diaspro, A., Bewersdorf, J., Hess, S. T., & Braeckmans, K. (2014). Precisely and accurately localizing single emitters in fluorescence microscopy. *Nature Methods*, *11*(3), 253–266. doi: 10.1038/nmeth.2843.

Dimiccoli, M., Jacob, J.-P., & Moisan, L. (2016). Particle detection and tracking in fluorescence time-lapse imaging: A contrario approach. *Machine Vision and Applications*, *27*, 511–527. doi: 10.1007/s00138-016-0757-7.

Egner, A., Andresen, V., & Hell, S. W. (2002). Comparison of the axial resolution of practical Nipkow-disk confocal fluorescence microscopy with that of multifocal multiphoton microscopy: Theory and experiment. *Journal of Microscopy*, *206*(1), 24–32. doi: 10.1046/j.1365-2818.2002.01001.x.

Fick, A. (1855). On liquid diffusion. *The London, Edinburgh, and Dublin Philosophical Magazine and Journal of Science*, *10*(63), 30–39. doi: 10.1080/14786445508641925.

Fish, D. A., Brinicombe, A. M., Pike, E. R., & Walker, J. G. (1995). Blind deconvolution by means of the Richardson–Lucy algorithm. *Journal of the Optical Society of America A*, *12*(1), 58–65. doi: 10.1364/JOSAA.12.000058.

Gal, N., Lechtman-Goldstein, D., & Weihs, D. (2013). Particle tracking in living cells: A review of the mean square displacement method and beyond. *Rheologica Acta*, *52*, 425–443. doi: 10.1007/s00397-013-0694-6.

Gonzalez, R. C., & Woods, R. E. (2002). *Digital image processing*. Upper Saddle River, N.J.: Prentice Hall.

Goulian, M., & Simon, S. M. (2000). Tracking single proteins within cells. *Biophysical Journal*, *79*(4), 2188–2198. doi: 10.1016/S0006-3495(00)76467-8.

Grimm, J. B., English, B. P., Chen, J., Slaughter, J. P., Zhang, Z., Revyakin, A., . . . Lavis, L. D. (2015). A general method to improve fluorophores for live-cell and single-molecule microscopy. *Nature Methods*, *12*(3), 244–250. doi: 10.1038/nmeth.3256.

Ha, T., & Tinnefeld, P. (2012). Photophysics of fluorescent probes for single-molecule biophysics and super-resolution imaging. *Annual Review of Physical Chemistry*, *63*, 595–617. doi: 10.1146/annurev-physchem-032210-103340.

Hecht, E. (2002). *Optics*. Reading, M.A.: Addison-Wesley.

Heddleston, J. M., & Chew, T. L. (2016). Light sheet microscopes: Novel imaging toolbox for visualizing life's processes. *International Journal of Biochemistry & Cell Biology*, *80*, 119–123. doi: 10.1016/j.biocel.2016.10.002.

Heid, P. J., Voss, E., & Soll, D. R. (2002). 3D-DIASemb: A computer-assisted system for reconstructing and motion analyzing in 4D every cell and nucleus in a developing embryo. *Developmental Biology*, *245*(2), 329–347. doi: 10.1006/dbio.2002.0631.

Hoogenboom, J. P., van Dijk, E. M., Hernando, J., van Hulst, N. F., & Garcia-Parajo, M. F. (2005). Power-law-distributed dark states are the main pathway for photobleaching of single organic molecules. *Physical Review Letters*, *95*(9), 097401. doi: 10.1103/PhysRevLett.95.097401.

Huang, B., Wang, W., Bates, M., & Zhuang, X. (2008). Three-dimensional super-resolution imaging by stochastic optical reconstruction microscopy. *Science*, *319*(5864), 810–813. doi: 10.1126/science.1153529.

Huisken, J., & Stainier, D. Y. R. (2009). Selective plane illumination microscopy techniques in developmental biology. *Development (Cambridge, England)*, *136*(12), 1963–1975. doi: 10.1242/dev.022426.

Huisken, J., Swoger, J., Del Bene, F., Wittbrodt, J., & Stelzer, E. H. K. (2004). Optical sectioning deep inside live embryos by selective plane illumination microscopy. *Science*, *305*(5686), 1007–1009. doi: 10.1126/science.1100035.

Jain, A. K. (1989). *Fundamentals of digital image processing*. Englewood Cliffs, NJ: Prentice Hall.

Jaqaman, K., & Danuser, G. (2009). Computational image analysis of cellular dynamics: A case study based on particle tracking. *Cold Spring Harbor Protocols*, *4*(12), pdb.top65. doi: 10.1101/pdb.top65.

Jaqaman, K., Loerke, D., Mettlen, M., Kuwata, H., Grinstein, S., Schmid, S. L., & Danuser, G. (2008). Robust single-particle tracking in live-cell time-lapse sequences. *Nature Methods*, *5*(8), 695–702. doi: 10.1038/nmeth.1237.

Ji, N., Shroff, H., Zhong, H., & Betzig, E. (2008). Advances in the speed and resolution of light microscopy. *Current Opinion in Neurobiology*, *18*(6), 605–616. doi: 10.1016/j.conb.2009.03.009.

Jin, H., Heller, D. A., Sharma, R., & Strano, M. S. (2009). Size-dependent cellular uptake and expulsion of single-walled carbon nanotubes: Single particle tracking and a generic uptake model for nanoparticles. *ACS Nano*, *3*(1), 149–158. doi: 10.1021/nn800532m.

Juette, M. F., Gould, T. J., Lessard, M. D., Mlodzianoski, M. J., Nagpure, B. S., Bennett, B. T., . . . Bewersdorf, J. (2008). Three-dimensional sub–100 nm resolution fluorescence microscopy of thick samples. *Nature Methods*, *5*, 527–529. doi: 10.1038/nmeth.1211.

Kaji, N., Tokeshi, M., & Baba, Y. (2007). Single-molecule measurements with a single quantum dot. *The Chemical Record*, *7*(5), 295–304. doi: 10.1002/tcr.20128.

Kalman, R. E. (1960). A new approach to linear filtering and prediction problems. *Journal of Basic Engineering*, *82*(1), 35–45. doi: 10.1115/1.3662552.

Keller, P. J., Schmidt, A. D., Wittbrodt, J., & Stelzer, E. H. K. (2008). Reconstruction of zebrafish early embryonic development by scanned light sheet microscopy. *Science*, *322*(5904), 1065–1069. doi: 10.1126/science.1162493.

Kreutzberger, A. J. B., Ji, M., Aaron, J., Mihaljević, L., & Urban, S. (2019). Rhomboid distorts lipids to break the viscosity-imposed speed limit of membrane diffusion. *Science*, *363*(6426), eaao0076. doi: 10.1126/science.aao0076.

Kubitscheck, U., Kückmann, O., Kues, T., & Peters, R. (2000). Imaging and tracking of single GFP molecules in solution. *Biophysical Journal*, *78*(4), 2170–2179. doi: 10.1016/S0006-3495(00)76764-6.

Kusumi, A., Nakada, C., Ritchie, K., Murase, K., Suzuki, K., Murakoshi, H., . . . Fujiwara, T. (2005). Paradigm shift of the plasma membrane concept from the two-dimensional continuum fluid to the partitioned fluid: High-speed single-molecule tracking of membrane molecules. *Annual Review of Biophysics and Biomolecular Structure*, *34*, 351–378. doi: 10.1146/annurev.biophys.34.040204.144637.

Kusumi, A., Sako, Y., & Yamamoto, M. (1993). Confined lateral diffusion of membrane receptors as studied by single particle tracking (nanovid microscopy). Effects of calcium-induced differentiation in cultured epithelial cells. *Biophysical Journal*, *65*(5), 2021–2040. doi: 10.1016/S0006-3495(93)81253-0.

Lambert, T. J., & Waters, J. C. (2017). Navigating challenges in the application of superresolution microscopy. *Journal of Cell Biology*, *216*(1), 53–63. doi: 10.1083/jcb.201610011.

Li, D., Shao, L., Chen, B. C., Zhang, X., Zhang, M., Moses, B., . . . Betzig, E. (2015). Extended-resolution structured illumination imaging of endocytic and cytoskeletal dynamics. *Science*, *349*(6251), aab3500. doi: 10.1126/science.aab3500.

Lin, G., Adiga, U., Olson, K., Guzowski, J. F., Barnes, C. A., & Roysam, B. (2003). A hybrid 3D watershed algorithm incorporating gradient cues and object models for automatic segmentation of nuclei in confocal image stacks. *Cytometry Part A*, *56*(1), 23–36. doi: 10.1002/cyto.a.10079.

Lippincott-Schwartz, J., & Patterson, G. H. (2003). Development and use of fluorescent protein markers in living cells. *Science*, *300*(5616), 87–91. doi: 10.1126/science.1082520.

Lucy, L. B. (1974). An iterative technique for the rectification of observed distributions. *Astronomical Journal*, *79*(6), 745–754. doi: 10.1086/111605.

Manzo, C., & Garcia-Parajo, M. F. (2015). A review of progress in single particle tracking: From methods to biophysical insights. *Reports on Progress in Physics*, *78*(12), 124601. doi: 10.1088/0034-4885/78/12/124601.

Marr, D., Hildreth, E., & Brenner, S. (1980). Theory of edge detection. *Proceedings of the Royal Society of London. Series B. Biological Sciences*, *207*(1167), 187–217. doi: 10.1098/rspb.1980.0020.

McDole, K., Guignard, L., Amat, F., Berger, A., Malandain, G., Royer, L. A., . . . Keller, P. J. (2018). In toto imaging and reconstruction of post-implantation mouse development at the single-cell level. *Cell*, *175*(3), 859–876. e833. doi: 10.1016/j.cell.2018.09.031.

Meijering, E. (2012). Cell segmentation: 50 years down the road. *IEEE Signal Processing Magazine*, *29*(5), 140–145. doi: 10.1109/MSP.2012.2204190.

Meijering, E., Dzyubachyk, O., & Smal, I. (2012). Methods for cell and particle tracking. *Methods in Enzymology*, *504*, 183–200. doi: 10.1016/B978-0-12-391857-4.00009-4.

Meijering, E., Smal, I., & Danuser, G. (2006). Tracking in molecular bioimaging. *IEEE Signal Processing Magazine*, *23*(3), 46–53. doi: 10.1109/MSP.2006.1628877.

Metzler, R., Jeon, J. H., Cherstvy, A. G., & Barkai, E. (2014). Anomalous diffusion models and their properties: Non-stationarity, non-ergodicity, and ageing at the centenary of single particle tracking. *Physical Chemistry Chemical Physics*, *16*(44), 24128–24164. doi: 10.1039/C4CP03465A.

Metzler, R., & Klafter, J. (2000). The random walk's guide to anomalous diffusion: A fractional dynamics approach. *Physics Reports*, *339*(1), 1–77. doi: 10.1016/S0370-1573(00)00070-3.

Michalet, X. (2010). Mean square displacement analysis of single-particle trajectories with localization error: Brownian motion in an isotropic medium. *Physical Review E*, *82*, 041914. doi: 10.1103/PhysRevE.82.041914.

Michalet, X., & Berglund, A. J. (2012). Optimal diffusion coefficient estimation in single-particle tracking. *Physical Review E*, *85*, 061916. doi: 10.1103/PhysRevE.85.061916.

Michel, R., Steinmeyer, R., Falk, M., & Harms, G. S. (2007). A new detection algorithm for image analysis of single, fluorescence-labeled proteins in living cells. *Microscopy*

Research and Technique, *70*(9), 763–770. doi: 10.1002/jemt.20485.

Monnier, N., Barry, Z., Park, H. Y., Su, K. C., Katz, Z., English, B. P., . . . Bathe, M. (2015). Inferring transient particle transport dynamics in live cells. *Nature Methods*, *12*(9), 838–840. doi: 10.1038/nmeth.3483.

Mortensen, K. I., Churchman, L. S., Spudich, J. A., & Flyvbjerg, H. (2010). Optimized localization analysis for single-molecule tracking and super-resolution microscopy. *Nature Methods*, *7*(5), 377–381. doi: 10.1038/nmeth.1447.

Mulmuley, K., Vazirani, U. V., & Vazirani, V. V. (1987). Matching is as easy as matrix inversion. In A. V. Aho (Ed.), *Proceedings of the 19th Annual ACM Symposium on Theory of Computing*. New York, NY: ACM. doi: 10.1145/28395.383347.

Neves, J. C., Castro, H., Tomás, A., Coimbra, M., & Proença, H. (2014). Detection and separation of overlapping cells based on contour concavity for Leishmania images. *Cytometry Part A*, *85*(6), 491–500. doi: 10.1002/cyto.a.22465.

Otsu, N. (1979). A threshold selection method from gray-level histograms. *IEEE Transactions on Systems, Man, and Cybernetics*, *9*(1), 62–66. doi: 10.1109/TSMC.1979.4310076.

Park, J. M., & Murphey, Y. L. (2008). Edge detection in grayscale, color, and range images. In B. W. Wah (Ed.), *Wiley Encyclopedia of Computer Science and Engineering*. Hoboken, NJ: John Wiley & Sons. doi: 10.1002/9780470050118.ecse603.

Parthasarathy, R. (2012). Rapid, accurate particle tracking by calculation of radial symmetry centers. *Nature Methods*, *9*, 724–726. doi: 10.1038/nmeth.2071.

Pavani, S. R. P., Thompson, M. A., Biteen, J. S., Lord, S. J., Liu, N., Twieg, R. J., . . . Moerner, W. E. (2009). Three-dimensional, single-molecule fluorescence imaging beyond the diffraction limit by using a double-helix point spread function. *Proceedings of the National Academy of Sciences*, *106*(9), 2995–2999. doi: 10.1073/pnas.0900245106.

Pawley, J. B. (2010). *Handbook of biological confocal microscopy*. New York: Springer Science & Business Media.

Pincus, Z., & Theriot, J. A. (2007). Comparison of quantitative methods for cell-shape analysis. *Journal of Microscopy*, *227*(2), 140–156. doi: 10.1111/j.1365-2818.2007.01799.x.

Pontes-Quero, S., Heredia, L., Casquero-García, V., Fernández-Chacón, M., Luo, W., Hermoso, A., . . . Benedito, R. (2017). Dual ifgMosaic: A versatile method for multispectral and combinatorial mosaic gene-function analysis. *Cell*, *170*(4), 800–814.e818. doi: 10.1016/j.cell.2017.07.031.

Prewitt, J. M. S., & Mendelsohn, M. L. (1966). The analysis of cell images. *Annals of the New York Academy of Sciences*, *128*(3), 1035–1053. doi: 10.1111/j.1749-6632.1965.tb11715.x.

Pun, T. (1980). A new method for grey-level picture thresholding using the entropy of the histogram. *Signal Processing*, *2*(3), 223–237. doi: 10.1016/0165-1684(80)90020-1.

Qi, X., Xing, F., Foran, D. J., & Yang, L. (2012). Robust segmentation of overlapping cells in histopathology specimens using parallel seed detection and repulsive level set. *IEEE Transactions on Biomedical Engineering*, *59*(3), 754–765. doi: 10.1109/TBME.2011.2179298.

Qian, H., Sheetz, M. P., & Elson, E. L. (1991). Single particle tracking. Analysis of diffusion and flow in two-dimensional systems. *Biophysical Journal*, *60*(4), 910–921. doi: 10.1016/S0006-3495(91)82125-7.

Rabut, G., & Ellenberg, J. (2004). Photobleaching techniques to study mobility and molecular dynamics of proteins in live cells: FRAP, iFRAP and FLIP. In R. D. Goldman, J. R. Swedlow, and D. L. Spector (Eds.), *Live cell imaging: A laboratory manual* (1 ed., pp. 101–126). Cold Spring Harbor, N.Y.: Cold Spring Harbor Laboratory Press.

Reid, D. (1979). An algorithm for tracking multiple targets. *IEEE Transactions on Automatic Control*, *24*(6), 843–854. doi: 10.1109/TAC.1979.1102177.

Richardson, W. H. (1972). Bayesian-based iterative method of image restoration. *Journal of the Optical Society of America*, *62*(1), 55–59. doi: 10.1364/JOSA.62.000055.

Roerdink, J. B. T. M., & Meijster, A. (2000). The watershed transform: Definitions, algorithms and parallelization strategies. *Fundamenta Informaticae*, *41*, 187–228. doi: 10.3233/FI-2000-411207.

Rothenberg, E., Sepúlveda, L. A., Skinner, S. O., Zeng, L., Selvin, P. R., & Golding, I. (2011). Single-virus tracking reveals a spatial receptor-dependent search mechanism. *Biophysical Journal*, *100*(12), 2875–2882. doi: 10.1016/j.bpj.2011.05.014.

Rueden, C. T., Schindelin, J., Hiner, M. C., DeZonia, B. E., Walter, A. E., Arena, E. T., & Eliceiri, K. W. (2017). ImageJ2: ImageJ for the next generation of scientific image data. *BMC Bioinformatics*, *18*(1), 529. doi: 10.1186/s12859-017-1934-z.

Ruthardt, N., Lamb, D. C., & Bräuchle, C. (2011). Single-particle tracking as a quantitative microscopy-based approach to unravel cell entry mechanisms of viruses and pharmaceutical nanoparticles. *Molecular Therapy*, *19*(7), 1199–1211. doi: 10.1038/mt.2011.102.

Ruusuvuori, P., Äijö, T., Chowdhury, S., Garmendia-Torres, C., Selinummi, J., Birbaumer, M., . . . Yli-Harja, O. (2010). Evaluation of methods for detection of fluorescence labeled subcellular objects in microscope images. *BMC Bioinformatics*, *11*, 248. doi: 10.1186/1471-2105-11-248.

Sato, S., Rancourt, A., Sato, Y., & Satoh, M. S. (2016). Single-cell lineage tracking analysis reveals that an established cell line comprises putative cancer stem cells and their heterogeneous progeny. *Scientific Reports*, *6*, 23328. doi: 10.1038/srep23328.

Saxton, M. J. (1994). Single-particle tracking: Models of directed transport. *Biophysical Journal*, *67*(5), 2110–2119. doi: 10.1016/S0006-3495(94)80694-0.

Saxton, M. J. (1995). Single-particle tracking: Effects of corrals. *Biophysical Journal*, *69*(2), 389–398. doi: 10.1016/S0006-3495(95)79911-8.

Saxton, M. J. (1997). Single-particle tracking: The distribution of diffusion coefficients. *Biophysical Journal*, *72*(3), 1744–1753. doi: 10.1016/S0006-3495(97)78820-9.

Saxton, M. J. (2009). Single-particle tracking. In T. Jue (Ed.), *Fundamental concepts in biophysics* (Vol. I, pp. 147–179). New York City, N.Y.: Humana Press.

Saxton, M. J., & Jacobson, K. (1997). Single-particle tracking: Applications to membrane dynamics. *Annual Review of Biophysics and Biomolecular Structure*, *26*, 373–399. doi: 10.1146/annurev.biophys.26.1.373.

Sbalzarini, I. F., & Koumoutsakos, P. (2005). Feature point tracking and trajectory analysis for video imaging in cell biology. *Journal of Structural Biology*, *151*(2), 182–195. doi: 10.1016/j.jsb.2005.06.002.

Schermelleh, L., Heintzmann, R., & Leonhardt, H. (2010). A guide to super-resolution fluorescence microscopy. *Journal of Cell Biology*, *190*(2), 165–175. doi: 10.1083/jcb.201002018.

Schindelin, J., Arganda-Carreras, I., Frise, E., Kaynig, V., Longair, M., Pietzsch, T., . . . Cardona, A. (2012). Fiji: An open-source platform for biological-image analysis. *Nature Methods*, *9*, 676–682. doi: 10.1038/nmeth.2019.

Schütz, G. J., Schindler, H., & Schmidt, T. (1997). Single-molecule microscopy on model membranes reveals anomalous diffusion. *Biophysical Journal*, *73*(2), 1073–1080. doi: 10.1016/S0006-3495(97)78139-6.

Seisenberger, G., Ried, M. U., Endress, T., Büning, H., Hallek, M., & Bräuchle, C. (2001). Real-time single-molecule imaging of the infection pathway of an adeno-associated virus. *Science*, *294*(5548), 1929–1932. doi: 10.1126/science.1064103.

Sezgin, M., & Sankur, B. (2004). Survey over image thresholding techniques and quantitative performance evaluation. *Journal of Electronic Imaging*, *13*(1), 146–165. doi: 10.1117/1.1631315.

Shao, L., Kner, P., Rego, E. H., & Gustafsson, M. G. (2011). Super-resolution 3D microscopy of live whole cells using structured illumination. *Nature Methods*, *8*(12), 1044–1046. doi: 10.1038/nmeth.1734.

Shtengel, G., Galbraith, J. A., Galbraith, C. G., Lippincott-Schwartz, J., Gillette, J. M., Manley, S., . . . Hess, H. F. (2009). Interferometric fluorescent super-resolution microscopy resolves 3D cellular ultrastructure. *Proceedings of the National Academy of Sciences*, *106*(9), 3125–3130. doi: 10.1073/pnas.0813131106.

Simson, R., Sheets, E. D., & Jacobson, K. (1995). Detection of temporary lateral confinement of membrane proteins using single-particle tracking analysis. *Biophysical Journal*, *69*(3), 989–993. doi: 10.1016/S0006-3495(95)79972-6.

Smal, I., Draegestein, K., Galjart, N., Niessen, W., & Meijering, E. (2008). Particle filtering for multiple object tracking in dynamic fluorescence microscopy images: Application to microtubule growth analysis. *IEEE Transactions on Medical Imaging*, *27*(6), 789–804. doi: 10.1109/TMI.2008.916964.

Smal, I., Loog, M., Niessen, W., & Meijering, E. (2010). Quantitative comparison of spot detection methods in fluorescence microscopy. *IEEE Transaction on Medical Imaging*, *29*(2), 282–301. doi: 10.1109/TMI.2009.2025127.

Snapp, E. (2005). Design and use of fluorescent fusion proteins in cell biology. *Current Protocols in Cell Biology*, *27*, 21.24.21–21.24.13. doi: 10.1002/0471143030.cb2104s27.

Sotak, G. E., & Boyer, K. L. (1989). The laplacian-of-gaussian kernel: A formal analysis and design procedure for fast, accurate convolution and full-frame output. *Computer Vision, Graphics, and Image Processing*, *48*(2), 147–189. doi: 10.1016/S0734-189X(89)80036-2.

Stegmaier, J., Amat, F., Lemon, W. C., McDole, K., Wan, Y., Teodoro, G., . . . Keller, P. J. (2016). Real-time three-dimensional cell segmentation in large-scale microscopy data of developing embryos. *Developmental Cell*, *36*(2), 225–240. doi: 10.1016/j.devcel.2015.12.028.

Sternberg, S. R. (1983). Biomedical image processing. *Computer*, *16*(1), 22–34. doi: 10.1109/MC.1983.1654163.

Takeda, H., Farsiu, S., & Milanfar, P. (2008). Deblurring using regularized locally adaptive kernel regression. *IEEE Transactions on Image Processing*, *17*(4), 550–563. doi: 10.1109/TIP.2007.918028.

Tassy, O., Daian, F., Hudson, C., Bertrand, V., & Lemaire, P. (2006). A quantitative approach to the study of cell shapes and interactions during early chordate embryogenesis. *Current Biology*, *16*(4), 345–358. doi: 10.1016/j.cub.2005.12.044.

Thompson, R. E., Larson, D. R., & Webb, W. W. (2002). Precise nanometer localization analysis for individual fluorescent probes. *Biophysical Journal*, *82*(5), 2775–2783. doi: 10.1016/S0006-3495(02)75618-X.

Tomer, R., Khairy, K., & Keller, P. J. (2011). Shedding light on the system: Studying embryonic development with light sheet microscopy. *Current Opinion in Genetics & Development*, *21*(5), 558–565. doi: 10.1016/j.gde.2011.07.003

Trimble, W. S., & Grinstein, S. (2015). Barriers to the free diffusion of proteins and lipids in the plasma membrane. *Journal of Cell Biology*, *208*(3), 259–271. doi: 10.1083/jcb.201410071.

Uhlen, M., Oksvold, P., Fagerberg, L., Lundberg, E., Jonasson, K., Forsberg, M., . . . Ponten, F. (2010). Towards a knowledge-based human protein atlas. *Nature Biotechnology*, *28*, 1248–1250. doi: 10.1038/nbt1210-1248.

van der Schaar, H. M., Rust, M. J., Chen, C., van der Ende-Metselaar, H., Wilschut, J., Zhuang, X., & Smit, J. M. (2008). Dissecting the cell entry pathway of dengue virus by single-particle tracking in living cells. *PLOS Pathogens*, *4*(12), e1000244. doi: 10.1371/journal.ppat.1000244.

Verkman, A. S. (2002). Solute and macromolecule diffusion in cellular aqueous compartments. *Trends in Biochemical Sciences*, *27*(1), 27–33. doi: 10.1016/S0968-0004(01)02003-5.

Vladimirov, N., Mu, Y., Kawashima, T., Bennett, D. V., Yang, C.-T., Looger, L. L., . . . Ahrens, M. B. (2014). Light-sheet functional imaging in fictively behaving zebrafish. *Nature Methods*, *11*, 883–884. doi: 10.1038/nmeth.3040.

Waters, J. C. (2013). Live-cell fluorescence imaging. *Methods in Cell Biology*, *114*, 125–150. doi: 10.1016/B978-0-12-407761-4.00006-3.

Wilson, R. S., Yang, L., Dun, A., Smyth, A. M., Duncan, R. R., Rickman, C., & Lu, W. (2016). Automated single particle detection and tracking for large microscopy datasets. *Royal Society Open Science*, *3*(5), 160225. doi: 10.1098/rsos.160225.

Winter, M. R., Mankowski, W., Wait, E., De La Hoz, E. C., Aguinaldo, A., & Cohen, A. R. (2018). Separating touching cells using pixel replicated elliptical shape models. *IEEE Transactions on Medical Imaging*, *38*(4), 883-893. doi: 10.1109/TMI.2018.2874104.

Winter, M. R., Mankowski, W., Wait, E., Temple, S., & Cohen, A. R. (2016). LEVER: Software tools for segmentation, tracking and lineaging of proliferating cells. *Bioinformatics*, *32*(22), 3530–3531. doi: 10.1093/bioinformatics/btw406.

Winter, M. R., Wait, E., Roysam, B., Goderie, S. K., Ali, R. A. N., Kokovay, E., . . . Cohen, A. R. (2011). Vertebrate neural stem cell segmentation, tracking and lineaging with validation and editing. *Nature Protocols*, *6*(12), 1942–1952. doi: 10.1038/nprot.2011.422.

Xing, F., & Yang, L. (2016). Robust nucleus/cell detection and segmentation in digital pathology and microscopy images: A comprehensive review. *IEEE Reviews in Biomedical Engineering*, *9*, 234–263. doi: 10.1109/RBME.2016.2515127.

Yildiz, A., Forkey, J. N., McKinney, S. A., Ha, T., Goldman, Y. E., & Selvin, P. R. (2003). Myosin V walks hand-over-hand: Single fluorophore imaging with 1.5-nm localization. *Science*, *300*(5628), 2061–2065. doi: 10.1126/science.1084398.

York, A. G., Chandris, P., Nogare, D. D., Head, J., Wawrzusin, P., Fischer, R. S., . . . Shroff, H. (2013). Instant super-resolution imaging in live cells and embryos via analog image processing. *Nature Methods*, *10*, 1122–1126. doi: 10.1038/nmeth.2687.

Zaritsky, A., Obolski, U., Gan, Z., Reis, C. R., Kadlecova, Z., Du, Y., . . . Danuser, G. (2017). Decoupling global biases and local interactions between cell biological variables. *Elife*, *6*, e22323. doi: 10.7554/eLife.22323.

Zhang, B., Zerubia, J., & Olivo-Marin, J.-C. (2007). Gaussian approximations of fluorescence microscope point-spread function models. *Applied Optics*, *46*(10), 1819–1829. doi: 10.1364/AO.46.001819.

Zimmer, C., Zhang, B., Dufour, A., Thebaud, A., Berlemont, S., Meas-Yedid, V., & Marin, J. O. (2006). On the digital trail of mobile cells. *IEEE Signal Processing Magazine*, *23*(3), 54–62. doi: 10.1109/MSP.2006.1628878.

Ziou, D., & Tabbone, S. (1998). Edge detection techniques: An overview. *International Journal of Pattern Recognition and Image Analysis*, *8*, 537–559. doi: 10.1.1.27.1821.